Plug-In Inversion: Model-Agnostic Inversion for Vision with Data Augmentations

Amin Ghiasi [*1] **Hamid Kazemi** [*1] **Steven Reich** [*1] **Chen Zhu** [1] **Micah Goldblum** [2] **Tom Goldstein** [1]

Abstract

Existing techniques for model inversion typically rely on hard-to-tune regularizers, such as total variation or feature regularization, which must be individually calibrated for each network in order to produce adequate images. In this work, we introduce Plug-In Inversion, which relies on a simple set of augmentations and does not require excessive hyper-parameter tuning. Under our proposed augmentation-based scheme, the same set of augmentation hyper-parameters can be used for inverting a wide range of image classification models, regardless of input dimensions or the architecture. We illustrate the practicality of our approach by inverting Vision Transformers (ViTs) and Multi-Layer Perceptrons (MLPs) trained on the ImageNet dataset, tasks which to the best of our knowledge have not been successfully accomplished by any previous works.

1. Introduction

Model inversion is an important tool for visualizing and interpreting behaviors inside neural architectures, understanding what models have learned, and explaining model behaviors. In general, model inversion seeks inputs that either activate a feature in the network (*feature visualization*) or yield a high output response for a particular class (*class inversion*) (Olah et al., 2017). Model inversion and visualization has been a cornerstone of conceptual studies that reveal how networks decompose images into semantic information (Zeiler & Fergus, 2014; Dosovitskiy & Brox, 2016). Over time, inversion methods have shifted from solving conceptual problems to solving practical ones. Saliency maps, for example, are image-specific model visualizations that reveal the inputs that most strong influence a model's decisions (Simonyan et al., 2014).

Recent advances in network architecture pose major challenges for existing model inversion schemes. Convolutional Neural Networks (CNN) have long been the de-facto approach for computer vision tasks, and are the focus of nearly all research in the model inversion field. Recently, other architectures have emerged that achieve results competitive with CNNs. These include Vision Transformers (ViTs; Dosovitskiy et al., 2021), which are based on self-attention layers, and MLP-Mixer (Tolstikhin et al., 2021) and ResMLP (Touvron et al., 2021a), which are based on Multi Layer Perceptron layers. Unfortunately, most existing model inversion methods either cannot be applied to these architectures, or are known to fail. For example, the feature regularizer used in DeepInversion (Yin et al., 2020) cannot be applied to ViTs or MLP-based models because they do not include Batch Normalization layers (Ioffe & Szegedy, 2015).

In this work, we focus on class inversion, the goal of which is to find interpretable images that maximize the score a classification model assigns to a chosen label without knowledge about the model's training data. Class inversion has been used for a variety of tasks including model interpretation (Mordvintsev et al., 2015), image synthesis (Santurkar et al., 2019; Kaur et al., 2019), and data-free knowledge transfer (Yin et al., 2020). However, current inversion methods have several key drawbacks. The quality of generated images is often highly sensitive to the weights assigned to regularization terms, so these hyper-parameters need to be carefully calibrated for each individual network. In addition, methods requiring batch norm parameters are not applicable to emerging architectures.

To overcome these limitations, we present *Plug-In Inversion* (*PII*), an augmentation-based approach to class inversion. *PII* does not require any explicit regularization, which eliminates the need to tune regularizer-specific hyper-parameters for each model or image instance. We show that *PII* is able to invert CNNs, ViTs, and MLP networks using the same architecture-agnostic method, and with the same architecture-agnostic hyper-parameters.

[*]Equal contribution [1]Department of Computer Science, University of Maryland, College Park, USA [2]New York University Center for Data Science, New York, USA. Correspondence to: Amin Ghiasi <ghiasi@umd.edu>, Hamid Kazemi <kazemira@umd.edu>.

Proceedings of the 39th International Conference on Machine Learning, Baltimore, Maryland, USA, PMLR 162, 2022.

Figure 1. Inverted images from a robust-ResNet50 model trained on ImageNet-1k.

We summarize our contributions as follows:

- We provide a detailed analysis of various augmentations and how they affect the quality of images produced via class inversion.
- We introduce *Plug-In Inversion* (*PII*), a new class inversion technique based on Centering, Zooming, ColorShift, and Ensembling. To the best of our knowledge, ColorShift and Centering are new augmentations that have not been used for model inversion prior to our work.
- We apply *PII* to dozens of different pre-trained models of varying architecture, justifying the claim that it can be 'plugged in' to most networks without modification.
- In particular, we show that *PII* succeeds in inverting ViTs and large MLP-based architectures, which to our knowledge has not previously been accomplished.
- Finally, we explore the potential for combining *PII* with prior methods.

2. Background

2.1. Class inversion

In the basic procedure for class inversion, we begin with a pre-trained model f and chosen target class y. We randomly initialize (and optionally pre-process) an image $\mathbf{x}$ in the input space of f. We then perform gradient descent to solve the optimization problem $\hat{x} = \arg\min_{\mathbf{x}} \mathcal{L}(f(\mathbf{x}), y)$ for a chosen objective function $\mathcal{L}$ to produce a class image $\hat{x}$. For very shallow networks and small datasets, letting $\mathcal{L}$ be cross-entropy or even the negative confidence assigned to the true class can produce recognizable images with minimal pre-processing (Fredrikson et al., 2015). Modern deep neural networks, however, cannot be inverted as easily.

2.2. Regularization

Most prior work on class inversion for deep networks has focused on carefully designing the objective function to produce quality images. This entails combining a divergence term (e.g. cross-entropy) with one or more regularization terms (*image priors*) meant to guide the optimization towards an image with 'natural' characteristics. *DeepDream* (Mordvintsev et al., 2015), following work on feature inversion (Mahendran & Vedaldi, 2015), uses two such terms: $\mathcal{R}_{\ell_2}(\mathbf{x}) = \|\mathbf{x}\|_2^2$, which penalizes the magnitude of the image vector, and total variation, defined as $\mathcal{R}_{TV}(\mathbf{x}) = \sum_{\substack{\Delta_i \in \{0,1\} \\ \Delta_j \in \{0,1\}}} \left(\sum_{i,j} (x_{i+\Delta_i, j+\Delta_j} - x_{i,j})^2\right)^{\frac{1}{2}}$, which penalizes sharp changes over small distances.

DeepInversion (Yin et al., 2020) uses both of these regularizers, along with the feature regularizer $\mathcal{R}_{feat}(\mathbf{x}) = \sum_k \left(\|\mu_k(\mathbf{x}) - \hat{\mu}_k\|_2 + \|\sigma_k^2(\mathbf{x}) - \hat{\sigma}_k^2\|_2\right)$, where μ_k, σ_k^2 are the batch mean and variance of the features output by the k-th convolutional layer, and $\hat{\mu}_k, \hat{\sigma}_k^2$ are corresponding Batch Normalization statistics stored in the model (Ioffe & Szegedy, 2015). Naturally, this method is only applicable to models that use Batch Normalization, which leaves out ViTs, MLPs, and even some CNNs. Furthermore, the optimal weights for each regularizer in the objective function vary wildly depending on architecture and training set, which presents a barrier to easily applying such methods to a wide array of networks.

2.3. Architectures for vision

We now present a brief overview of the three basic types of vision architectures that we will consider.

Convolutional Neural Networks (CNNs) have long been the standard in deep learning for computer vision (LeCun et al., 1989; Krizhevsky et al., 2012). Convolutional layers encourage a model to learn properties desirable for vision tasks, such as translation invariance. Numerous CNN models exist, mainly differing in the number, size, and ar-

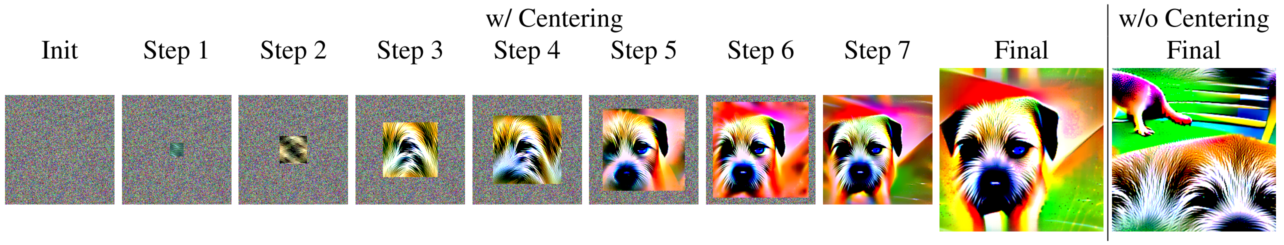

Figure 2. An image at different stages of optimization with centering (left), and an image inverted without centering (right), for the Border Terrier class of a robust ResNet-50.

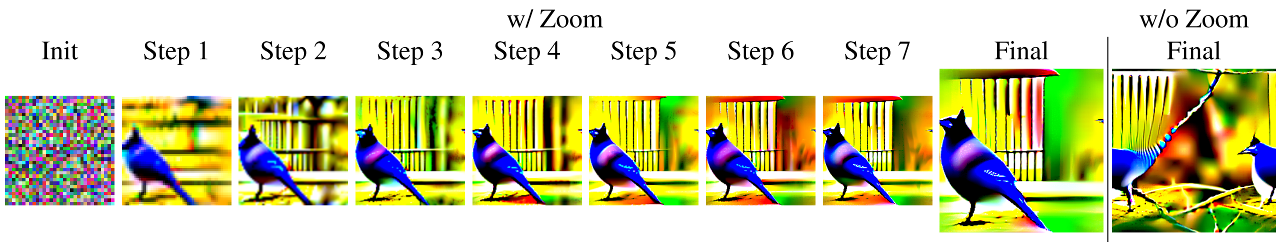

Figure 3. An image during different stages of optimization with zoom (left), and an image inverted without zoom (right), for the Jay class of a robust ResNet-50.

rangement of convolutional blocks and whether they include residual connections, Batch Normalization, or other modifications (He et al., 2016; Zagoruyko & Komodakis, 2016; Simonyan & Zisserman, 2014).

Dosovitskiy et al. (2021) recently introduced **Vision Transformers** (ViTs), adapting the Transformer architectures commonly used in NLP (Vaswani et al., 2017). ViTs break input images into patches, combine them with positional embeddings, and use these as input tokens to self-attention modules. Some proposed variants require less training data (Touvron et al., 2021c), have convolutional inductive biases (d'Ascoli et al., 2021), or make other modifications to the attention modules (Chu et al., 2021; Liu et al., 2021b; Xu et al., 2021).

Subsequently, a number of authors have proposed vision models which are based solely on **Multi-Layer Perceptrons** (MLPs), using insights from ViTs (Tolstikhin et al., 2021; Touvron et al., 2021a; Liu et al., 2021a). Generally, these models use patch embeddings similar to ViTs and alternate channel-wise and patch-wise linear embeddings, along with non-linearities and normalization.

We emphasize that as the latter two architecture types are recent developments, our work is the first to study them in the context of model inversion.

3. Plug-In Inversion

Prior work on class inversion uses augmentations like jitter, which randomly shifts an image horizontally and vertically, and horizontal flips to improve the quality of inverted images (Mordvintsev et al., 2015; Yin et al., 2020). The hypothesis behind their use is that different views of the same image should result in similar scores for the target class. These augmentations are applied to the input before feeding it to the network, and different augmentations are used for each gradient step used to reconstruct x. In this section, we explore additional augmentations that benefit inversion before describing how we combine them to form the *PII* algorithm.

As robust models are typically easier to invert than naturally trained models (Tsipras et al., 2018; Santurkar et al., 2019; Mejia et al., 2019; Kaur et al., 2019), we use a robust ResNet-50 (He et al., 2016) model trained on the ImageNet (Deng et al., 2009) dataset throughout this section as a toy example to examine how different augmentations impact inversion. Note, we perform the demonstrations in this section under slightly different conditions and with different models than those ultimately used for *PII* in order to highlight the effects of the augmentations as clearly as possible. The reader may find thorough experimental details in the appendix, section C. A few examples of the resulting inverted images can be found in 1.

3.1. Restricting Search Space

In this section, we consider two augmentations to improve the spatial qualities of inverted images: *Centering* and *Zoom*. These are designed based on our hypothesis that restricting the input optimization space encourages better placement of recognizable features. Both methods start with small input patches, and each gradually increases this

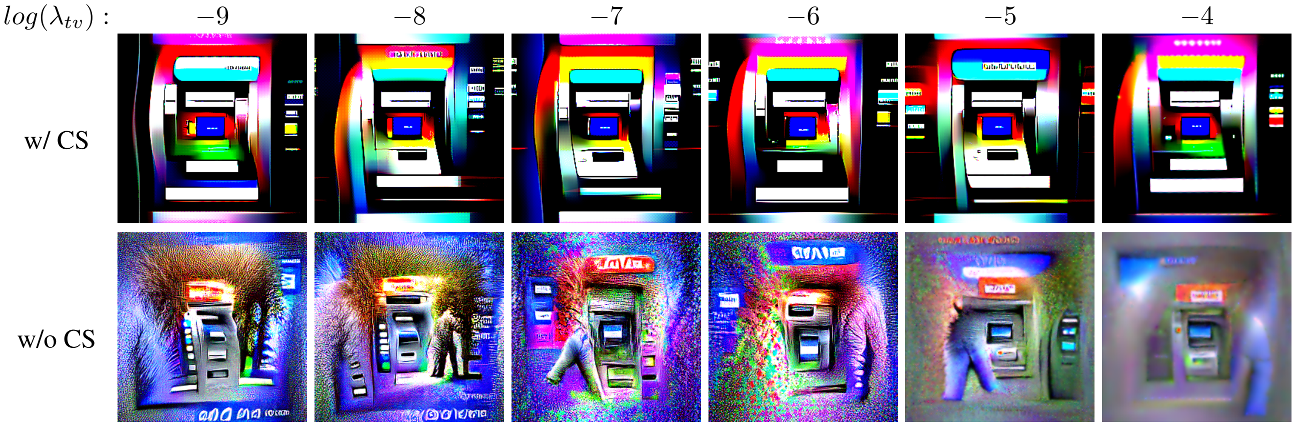

Figure 4. Inversions of the robust ResNet-50 ATM class, with and without ColorShift and with varying TV regularization strength. The inversion process with ColorShift is robust to changes in the λ_{tv} hyper-parameter, while without it, λ_{tv} seems to present a trade-off between noise and blur.

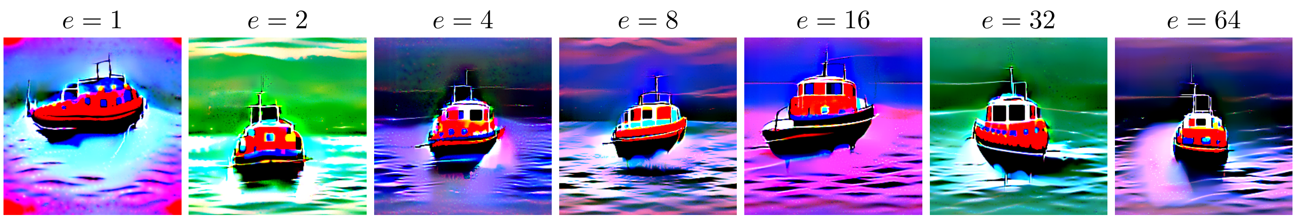

Figure 5. Effect of ensemble size in the quality of inverted images for the Tugboat class of a robust ResNet-50.

space in different ways to reach the intended input size. In doing so, they force the inversion algorithm to place important semantic content in the center of the image.

Centering Let x be the input image being optimized. At first, we only optimize a patch at the center of x. After a fixed number of iterations, we increase the patch size outward by padding with random noise, repeating this until the patch reaches the full input size. Figure 2 shows the state of the image prior at each stage of this process, as well as an image produced without centering. Without centering, the shift invariance of the networks allows most semantic content to scatter to the image edges. With centering, results remain coherent.

Zoom For zoom, we begin with an image x of lower resolution than the desired result. In each step, we optimize this image for a fixed number of iterations and then up-sample the result, repeating until we reach the full resolution. Figure 3 shows the state of an image at each step of the zoom procedure, along with an image produced without zoom. The latter image splits the object of interest at its edges. By contrast, zoom appears to find a meaningful structure for the image in the early steps and refines details like texture as the resolution increases.

We note that zoom is not an entirely novel idea in inversion. Yin et al. (2020) use a similar technique as 'warm-up' for better performance and speed-up. However, we observe that continuing zoom throughout optimization contributes to the overall success of *PII*.

Zoom + Centering Unsurprisingly, we have found that applying zoom and centering simultaneously yields even better results than applying either individually, since each one provides a different benefit. Centering places detailed and important features (e.g. the dog's eye in Figure 2) near the center and builds the rest of the image around the existing patch. Zoom helps enforce a sound large-scale structure for the image and fills in details later.

The combined Zoom and Centering process proceeds in 'stages', each at a higher resolution than the last. Each stage begins with an image patch generated by the previous stage, which approximately minimizes the inversion loss. The patch is then up-sampled to a resolution halfway between the previous stage and current stage resolution, filling the center of the image and leaving a border which is padded with random noise. The next round of optimization then begins starting from this newly processed image.

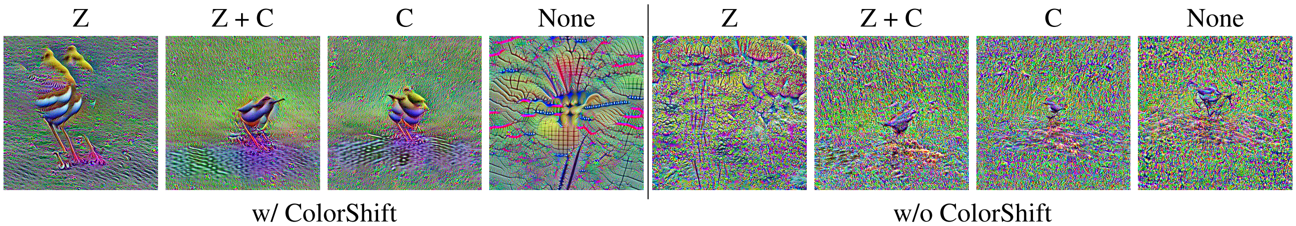

Figure 6. The effect of various combinations of zoom, centering, and ColorShift when inverting the Dipper class using a *naturally*-trained ResNet-50.

3.2. ColorShift Augmentation

The colors of the illustrative images we have shown so far are notably different from what one might expect in a natural image. This is due to *ColorShift*, a new augmentation that we now present.

ColorShift is an adjustment of an image's colors by a random mean and variance in each channel. This can be formulated as follows:

$$\text{ColorShift}(\mathbf{x}) = \sigma \mathbf{x} - \mu,$$

where μ and σ are C-dimensional[1] vectors drawn from $\mathcal{U}(-\alpha, \alpha)$ and $e^{\mathcal{U}(-\beta,\beta)}$, respectively, and are repeatedly redrawn after a fixed number of iterations. We use $\alpha = \beta = 1.0$ in all demonstrations unless otherwise noted. At first glance, this deliberate shift away from the distribution of natural images seems counterproductive to the goal of producing a recognizable image. However, our results show that using ColorShift noticeably increases the amount of visual information in inverted images and also obviates the need for hard-to-tune regularizers to stabilize optimization.

We visualize the stabilizing effect of ColorShift in Figure 4. In this experiment, we invert the model by minimizing the sum of a cross entropy and a total-variation (TV) penalty. Without ColorShift, the quality of images is highly dependent on the weight λ_{TV} of the TV regularizer; smaller values produce noisy images, while larger values produce blurry ones. Inversion with ColorShift, on the other hand, is insensitive to this value and in fact succeeds when omitting the regularizer altogether.

Other preliminary experiments show that ColorShift similarly removes the need for ℓ_2 or feature regularization, as our main results for *PII* will show. We conjecture that by forcing unnatural colors into an image, ColorShift requires the optimization to find a solution which contains meaningful semantic information, rather than photo-realistic colors, in order to achieve a high class score. Alternatively, as seen in Figure 11, images optimized with an image prior may achieve high scores despite a lack of semantic information merely by finding sufficiently natural colors and textures.

[1] C being the number of channels

3.3. Ensembling

Ensembling is an established tool often used in applications including enhanced inference (Opitz & Maclin, 1999), dataset security (Souri et al., 2021), generating real-world adversarial examples (Athalye et al., 2018; Eykholt et al., 2018) and model inversion (Kaur et al., 2019). Using randomized smoothing, (Kaur et al., 2019) shows that ensembling different views of the same image improves the quality of inverted images. Similarly, we find that optimizing an ensemble composed of different ColorShifts of the same image simultaneously improves the performance of inversion methods. To this end, we minimize the average of cross-entropy losses $\mathcal{L}(f(\mathbf{x}_i), y)$, where the $\mathbf{x}_i$ are different ColorShifts of the image at the current step of optimization. Figure 5 shows the result of applying ensembling alongside ColorShift. We observe that larger ensembles appear to give slight improvements, but even ensembles of size 1 or two produce satisfactory results. This is important for models like ViTs, where available GPU memory constrains the possible size of this ensemble; in general, we use the largest ensemble size (up to a maximum of $e = 32$) that our hardware permits for a particular model. More results on the effect of ensemble size can be found in Figure 16. We show the effect of ensembling using other well-known augmentations and compare them to ColorShift in Appendix Section A.6, and observe that ColorShift is the strongest among augmentations we tried for model inversion.

3.4. The Plug-in Inversion Method

We combine the jitter, ensembling, ColorShift, centering, and zoom techniques, and name the result Plug-In Inversion, which references the ability to 'plug in' any differentiable model, including ViTs and MLPs, using a single fixed set of hyper-parameters. Full pseudocode for the algorithm may be found in appendix E. In the next section, we detail the experimental method that we used to find these hyper-parameters, after which we present our main results.

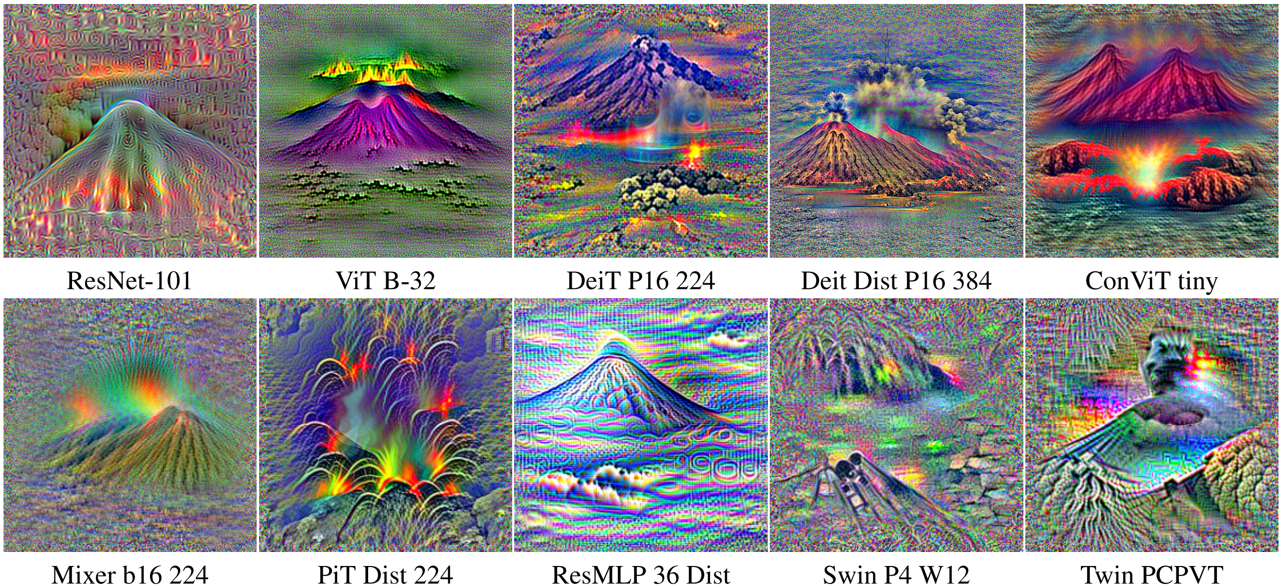

Figure 7. Images inverted from the ImageNet Volcano class for various Convolutional, Transformer, and MLP-based networks using *PII*. See figure 18 for further examples. For more details about networks, refer to Appendix B.

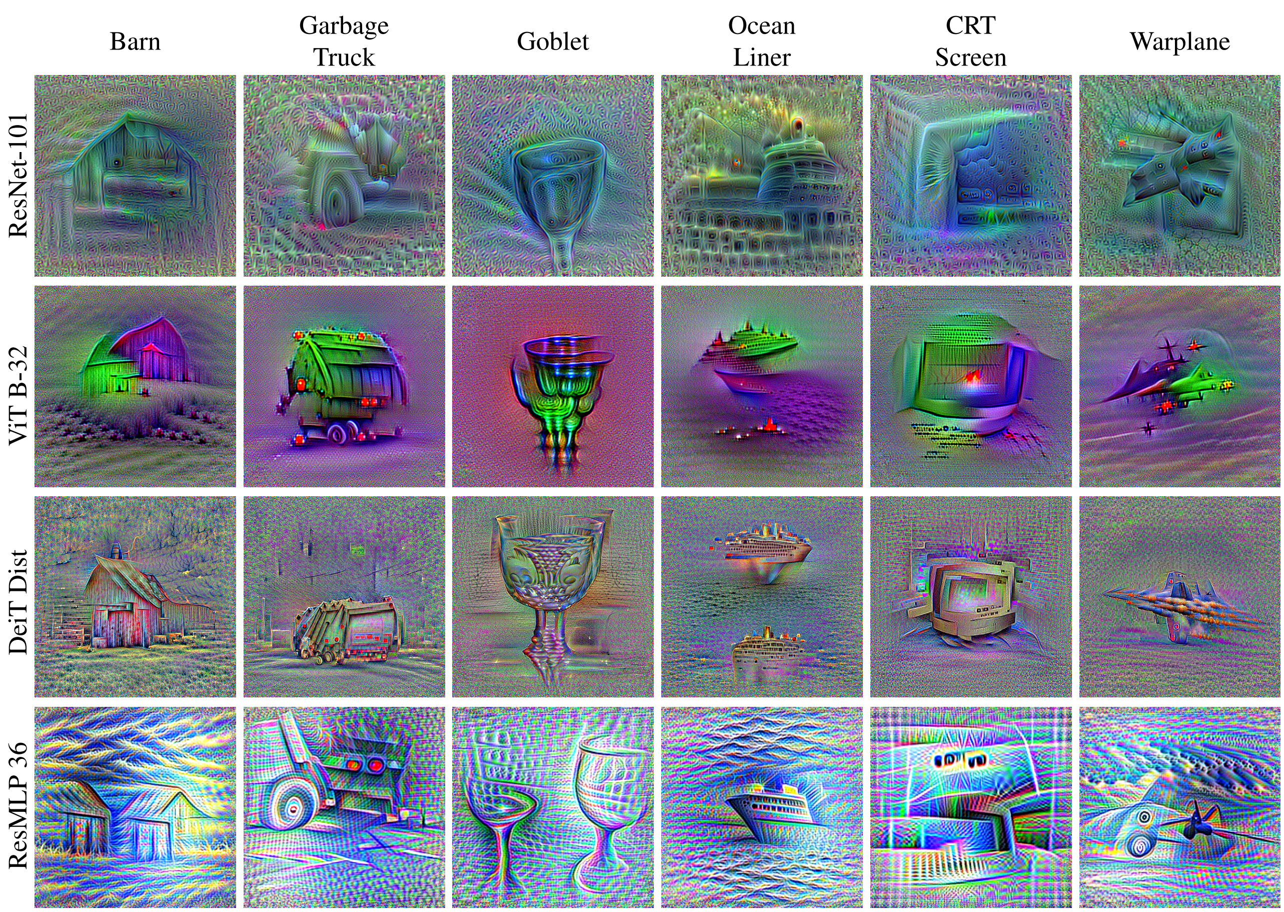

Figure 8. Inverting different ImageNet model and class combinations for different classes using *PII*.

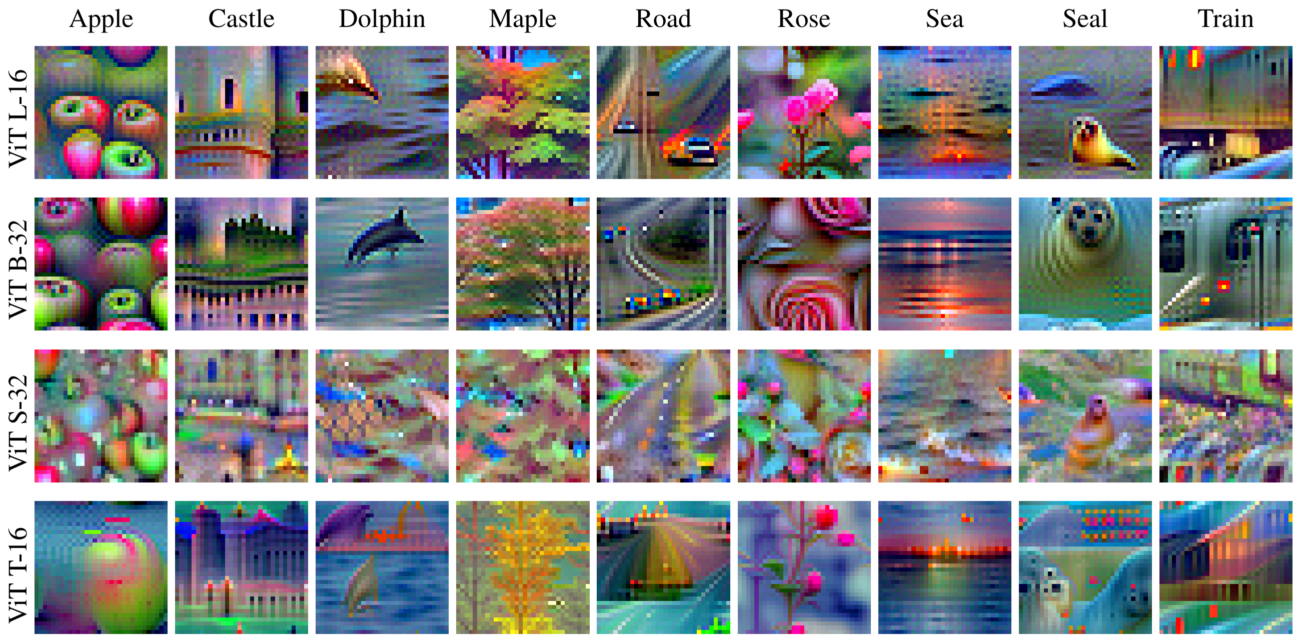

Figure 9. Inverting different CIFAR-100 model and class combinations using *PII*.

4. Experimental Setup

In order to tune hyper-parameters of *PII* for use on naturally-trained models, we use the `torchvision` (Paszke et al., 2019) ImageNet-trained ResNet-50 model. We apply centering + zoom simultaneously in 7 'stages'. During each stage, we optimize the selected patch for 400 iterations, applying random jitter and ColorShift at each step. We use the Adam (Kingma & Ba, 2014) optimizer with momentum $\beta_m = (0.5, 0.99)$, initial learning rate $lr = 0.01$, and cosine-decay. At the beginning of every stage, the learning rate and optimizer are re-initialized. We use $\alpha = \beta = 1.0$ for the ColorShift parameters, and an ensemble size of $e = 32$. Further ablation studies for these choices can be found in figures 12, 15, and 16.

All the models (including pre-trained weights) we consider in this work are publicly available from widely-used sources. Explicit details of model resources can be found in section B of the appendix. We also make the code used for all demonstrations and experiments in this work available at `https://github.com/youranonymousefriend/plugininversion`.

5. Results

5.1. *PII* works on a range of architectures

We now present the results of applying Plug-In Inversion to different types of models. We once again emphasize that we use identical settings for the *PII* parameters in all cases.

Figure 7 depicts images produced by inverting the Volcano class for a variety of architectures, including examples of CNNs, ViTs, and MLPs. While the quality of images varies somewhat between networks, all of them include distinguishable and well-placed visual information. Many more examples are found in Figure 18 of the Appendix.

In Figure 8, we show images produced by *PII* from representatives of each main type of architecture for a few arbitrary ImageNet classes. We note the distinct visual styles that appear in each row, which supports the perspective of model inversion as a tool for understanding what kind of information different networks learn during training.

5.2. *PII* works on other datasets

In Figure 9, we use *PII* to invert ViT models trained on ImageNet and fine-tuned on CIFAR-100. Figure 10 shows inversion results from models fine-tuned on CIFAR-10. We emphasize that these were produced using identical settings to the ImageNet results above, whereas other methods (like DeepInversion) tune dataset-specific hyperparameters.

5.3. Comparing *PII* to existing methods

To quantitatively evaluate our method, we invert both a pretrained ViT model and a pretrained ResMLP model to produce one image per class using *PII*, and do the same using DeepDream (i.e., DeepInversion minus feature regularization, which is not available for this model). We then use a variety of pre-trained models to classify these images. Ta-

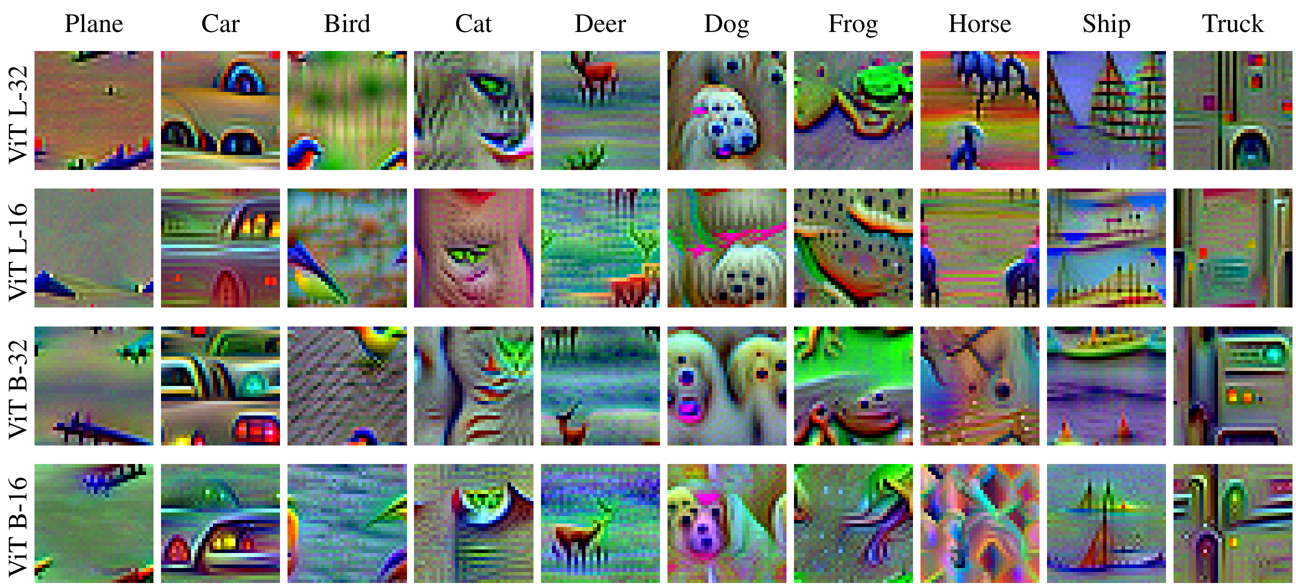

Figure 10. Inverting different every class of CIFAR-10 from different ViT models using *PII*.

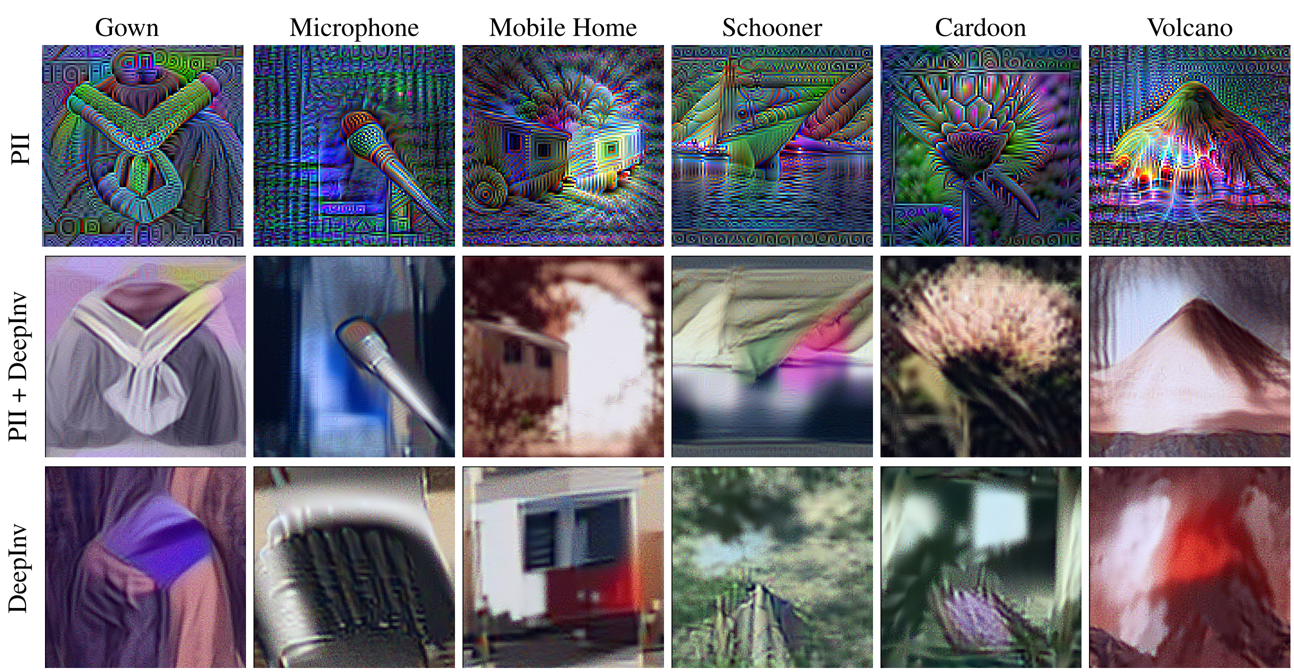

Figure 11. PII and DeepInversion results for a naturally-trained ResNet-50. The middle row represents performing *PII* and using the result as an initialization for DeepInversion.

ble 2 contains the mean top-1 and top-5 classification accuracies across these models, as well as Inception scores, for the generated images from each method. We see that our method is competitive with, and in the ViT case widely outperforms, DeepDream. Appendix G contains more details about these experiments.

Figure 11 shows images from a few arbitrary classes produced by *PII* and DeepInversion. We additionally show images produced by DeepInversion using the output of *PII*, rather than random noise, as its initialization. Using either initialization, DeepInversion clearly produces images with natural-looking colors and textures, which *PII* of course does not. However, DeepInversion alone results in some images that either do not clearly correspond to the target

Table 1. Inception score and mean classification accuracies of various models on images inverted from (a) ViT B-32 and (b) ResMLP 36 by *PII* and DeepDream. Higher is better in all fields.

Method	Inception score	Top-1	Top-5
PII	28.17 ± 7.21	77.0%	89.5%
DeepDream	2.72 ± 0.23	35.2%	49.6%

(a) Images inverted from ViT B-32

Method	Inception score	Top-1	Top-5
PII	6.79 ± 2.18	49.2%	62.0%
DeepDream	3.27 ± 0.47	51.3%	61.3%

(b) Images inverted from ResMLP 36

class or are semantically confusing. By comparison, *PII* again produces images with strong spatial and semantic qualities. Interestingly, these qualities appear to be largely retained when applying DeepInversion after *PII*, but with the color and texture improvements that image priors afford (Mahendran & Vedaldi, 2015), suggesting that using these methods in tandem may be a way to produce even better inverted images from CNNs than either method independently.

Additionally, we compare PII to DeepInversion for knowledge-free distillation task (Yin et al., 2020). Please note that (Yin et al., 2020) generates images that maximize the mismatch between the teacher and student *in every training iteration*. As a result, the setting described in DeepInversion is computationally expensive. For our comparison, we instead generate a fixed set of training samples for each method, and perform knowledge distillation with data augmentations on this set. The results are shown in Table 2.

Methods	1000	2000	3000	4000
DI	86.46%	88.86%	89.86%	90.11%
PII(Z) + DI	**86.52**%	**89.12**%	**90.24**%	**91.23**%
PII(Z+C) + DI	85.91%	88.98%	89.84%	90.62%
PII(C) + DI	84.68%	88.20%	89.53%	90.53%

Table 2. Accuracy of the student network on the CIFAR10 dataset. Higher is better. Teacher: ResNet20 (92.6% test acc), Student: ResNet18

In Table 2, each column shows the students best accuracy using different number of examples per class. We observe that when we have fewer number of examples, DeepInversion(DI) and PII + DI (applying DeepInversion after PII) have similar performance. However, PII + DI performs better when we have more examples, demonstrating that PII can be complementary to DI and generate images that lead to higher accuracy.

Appendix F contains additional qualitative comparisons to DeepDream and DeepInversion, further illustrating the need for model-specific hyperparameter tuning in contrast to our method.

6. Conclusion

We studied the effect of various augmentations on the quality of class-inverted images and introduced Plug-In Inversion, which uses these augmentations in tandem. We showed that this technique produces intelligible images from a wide range of well-studied architectures and datasets, including the recently introduced ViTs and MLPs, without a need for model-specific hyper-parameter tuning. We believe that augmentation-based model inversion is a promising direction for future research in understanding computer vision models.

7. Acknowledgement

This work was supported by the ONR MURI Program, the National Science Foundation DMS-1912866, and DARPA GARD.

References

Athalye, A., Engstrom, L., Ilyas, A., and Kwok, K. Synthesizing robust adversarial examples. In *International conference on machine learning*, pp. 284–293. PMLR, 2018.

Chen, X., Fan, H., Girshick, R., and He, K. Improved baselines with momentum contrastive learning. *arXiv preprint arXiv:2003.04297*, 2020.

Chu, X., Tian, Z., Wang, Y., Zhang, B., Ren, H., Wei, X., Xia, H., and Shen, C. Twins: Revisiting the design of spatial attention in vision transformers. *arXiv preprint arXiv:2104.13840*, 1(2):3, 2021.

d'Ascoli, S., Touvron, H., Leavitt, M., Morcos, A., Biroli, G., and Sagun, L. Convit: Improving vision transformers with soft convolutional inductive biases. *arXiv preprint arXiv:2103.10697*, 2021.

Deng, J., Dong, W., Socher, R., Li, L.-J., Li, K., and Fei-Fei, L. Imagenet: A large-scale hierarchical image database. In *2009 IEEE conference on computer vision and pattern recognition*, pp. 248–255. Ieee, 2009.

Dosovitskiy, A. and Brox, T. Inverting visual representations with convolutional networks. In *Proceedings of the IEEE conference on computer vision and pattern recognition*, pp. 4829–4837, 2016.

Dosovitskiy, A., Beyer, L., Kolesnikov, A., Weissenborn, D., Zhai, X., Unterthiner, T., Dehghani, M., Minderer, M., Heigold, G., Gelly, S., Uszkoreit, J., and Houlsby, N. An image is worth 16x16 words: Transformers for image recognition at scale, 2021.

Eykholt, K., Evtimov, I., Fernandes, E., Li, B., Rahmati, A., Xiao, C., Prakash, A., Kohno, T., and Song, D. Robust physical-world attacks on deep learning visual classification. In *Proceedings of the IEEE conference on computer vision and pattern recognition*, pp. 1625–1634, 2018.

Fredrikson, M., Jha, S., and Ristenpart, T. Model inversion attacks that exploit confidence information and basic countermeasures. In *Proceedings of the 22nd ACM SIGSAC conference on computer and communications security*, pp. 1322–1333, 2015.

He, K., Zhang, X., Ren, S., and Sun, J. Deep residual learning for image recognition. In *Proceedings of the IEEE conference on computer vision and pattern recognition*, pp. 770–778, 2016.

Heo, B., Yun, S., Han, D., Chun, S., Choe, J., and Oh, S. J. Rethinking spatial dimensions of vision transformers. *arXiv preprint arXiv:2103.16302*, 2021.

Howard, A., Sandler, M., Chu, G., Chen, L.-C., Chen, B., Tan, M., Wang, W., Zhu, Y., Pang, R., Vasudevan, V., et al. Searching for mobilenetv3. In *Proceedings of the IEEE/CVF International Conference on Computer Vision*, pp. 1314–1324, 2019.

Huang, G., Liu, Z., Van Der Maaten, L., and Weinberger, K. Q. Densely connected convolutional networks. In *Proceedings of the IEEE conference on computer vision and pattern recognition*, pp. 4700–4708, 2017.

Iandola, F. N., Han, S., Moskewicz, M. W., Ashraf, K., Dally, W. J., and Keutzer, K. Squeezenet: Alexnet-level accuracy with 50x fewer parameters and¡ 0.5 mb model size. *arXiv preprint arXiv:1602.07360*, 2016.

Ioffe, S. and Szegedy, C. Batch normalization: Accelerating deep network training by reducing internal covariate shift. In *International conference on machine learning*, pp. 448–456. PMLR, 2015.

Kaur, S., Cohen, J., and Lipton, Z. C. Are perceptually-aligned gradients a general property of robust classifiers? *arXiv preprint arXiv:1910.08640*, 2019.

Kingma, D. P. and Ba, J. Adam: A method for stochastic optimization. *arXiv preprint arXiv:1412.6980*, 2014.

Krizhevsky, A., Sutskever, I., and Hinton, G. E. Imagenet classification with deep convolutional neural networks. *Advances in neural information processing systems*, 25: 1097–1105, 2012.

LeCun, Y., Boser, B., Denker, J. S., Henderson, D., Howard, R. E., Hubbard, W., and Jackel, L. D. Backpropagation applied to handwritten zip code recognition. *Neural computation*, 1(4):541–551, 1989.

Liu, H., Dai, Z., So, D. R., and Le, Q. V. Pay attention to mlps. *arXiv preprint arXiv:2105.08050*, 2021a.

Liu, Z., Lin, Y., Cao, Y., Hu, H., Wei, Y., Zhang, Z., Lin, S., and Guo, B. Swin transformer: Hierarchical vision transformer using shifted windows. *arXiv preprint arXiv:2103.14030*, 2021b.

Ma, N., Zhang, X., Zheng, H.-T., and Sun, J. Shufflenet v2: Practical guidelines for efficient cnn architecture design. In *Proceedings of the European conference on computer vision (ECCV)*, pp. 116–131, 2018.

Mahendran, A. and Vedaldi, A. Understanding deep image representations by inverting them. In *Proceedings of the IEEE conference on computer vision and pattern recognition*, pp. 5188–5196, 2015.

Mejia, F. A., Gamble, P., Hampel-Arias, Z., Lomnitz, M., Lopatina, N., Tindall, L., and Barrios, M. A. Robust or private? adversarial training makes models more vulnerable to privacy attacks. *arXiv preprint arXiv:1906.06449*, 2019.

Mordvintsev, A., Olah, C., and Tyka, M. Inceptionism: Going deeper into neural networks. 2015.

Olah, C., Mordvintsev, A., and Schubert, L. Feature visualization. *Distill*, 2017. doi: 10.23915/distill.00007. https://distill.pub/2017/feature-visualization.

Opitz, D. and Maclin, R. Popular ensemble methods: An empirical study. *Journal of artificial intelligence research*, 11:169–198, 1999.

Paszke, A., Gross, S., Massa, F., Lerer, A., Bradbury, J., Chanan, G., Killeen, T., Lin, Z., Gimelshein, N., Antiga, L., et al. Pytorch: An imperative style, high-performance deep learning library. *Advances in neural information processing systems*, 32:8026–8037, 2019.

Salimans, T., Goodfellow, I., Zaremba, W., Cheung, V., Radford, A., and Chen, X. Improved techniques for training gans. *Advances in neural information processing systems*, 29:2234–2242, 2016.

Sandler, M., Howard, A., Zhu, M., Zhmoginov, A., and Chen, L.-C. Mobilenetv2: Inverted residuals and linear bottlenecks. In *Proceedings of the IEEE conference on computer vision and pattern recognition*, pp. 4510–4520, 2018.

Santurkar, S., Ilyas, A., Tsipras, D., Engstrom, L., Tran, B., and Madry, A. Image synthesis with a single (robust) classifier. *Advances in Neural Information Processing Systems*, 32:1262–1273, 2019.

Shafahi, A., Najibi, M., Ghiasi, A., Xu, Z., Dickerson, J., Studer, C., Davis, L. S., Taylor, G., and Goldstein, T. Adversarial training for free! *arXiv preprint arXiv:1904.12843*, 2019.

Simonyan, K. and Zisserman, A. Very deep convolutional networks for large-scale image recognition. *arXiv preprint arXiv:1409.1556*, 2014.

Simonyan, K., Vedaldi, A., and Zisserman, A. Deep inside convolutional networks: Visualising image classification models and saliency maps, 2014.

Souri, H., Goldblum, M., Fowl, L., Chellappa, R., and Goldstein, T. Sleeper agent: Scalable hidden trigger backdoors for neural networks trained from scratch. *arXiv preprint arXiv:2106.08970*, 2021.

Szegedy, C., Liu, W., Jia, Y., Sermanet, P., Reed, S., Anguelov, D., Erhan, D., Vanhoucke, V., and Rabinovich, A. Going deeper with convolutions. In *Proceedings of the IEEE conference on computer vision and pattern recognition*, pp. 1–9, 2015.

Tan, M., Chen, B., Pang, R., Vasudevan, V., Sandler, M., Howard, A., and Le, Q. V. Mnasnet: Platform-aware neural architecture search for mobile. In *Proceedings of the IEEE/CVF Conference on Computer Vision and Pattern Recognition*, pp. 2820–2828, 2019.

Tolstikhin, I., Houlsby, N., Kolesnikov, A., Beyer, L., Zhai, X., Unterthiner, T., Yung, J., Keysers, D., Uszkoreit, J., Lucic, M., et al. Mlp-mixer: An all-mlp architecture for vision. *arXiv preprint arXiv:2105.01601*, 2021.

Touvron, H., Bojanowski, P., Caron, M., Cord, M., El-Nouby, A., Grave, E., Izacard, G., Joulin, A., Synnaeve, G., Verbeek, J., and Jégou, H. Resmlp: Feedforward networks for image classification with data-efficient training, 2021a.

Touvron, H., Cord, M., Douze, M., Massa, F., Sablayrolles, A., and Jegou, H. Training data-efficient image transformers & distillation through attention. In *International Conference on Machine Learning*, volume 139, pp. 10347–10357, July 2021b.

Touvron, H., Cord, M., Douze, M., Massa, F., Sablayrolles, A., and Jégou, H. Training data-efficient image transformers & distillation through attention. In *International Conference on Machine Learning*, pp. 10347–10357. PMLR, 2021c.

Tsipras, D., Santurkar, S., Engstrom, L., Turner, A., and Madry, A. Robustness may be at odds with accuracy. *arXiv preprint arXiv:1805.12152*, 2018.

Vaswani, A., Shazeer, N., Parmar, N., Uszkoreit, J., Jones, L., Gomez, A. N., Kaiser, Ł., and Polosukhin, I. Attention is all you need. In *Advances in neural information processing systems*, pp. 5998–6008, 2017.

Wightman, R. Pytorch image models. https://github.com/rwightman/pytorch-image-models, 2019.

Xie, S., Girshick, R., Dollár, P., Tu, Z., and He, K. Aggregated residual transformations for deep neural networks. In *Proceedings of the IEEE conference on computer vision and pattern recognition*, pp. 1492–1500, 2017.

Xu, W., Xu, Y., Chang, T., and Tu, Z. Co-scale conv-attentional image transformers. *arXiv preprint arXiv:2104.06399*, 2021.

Yin, H., Molchanov, P., Alvarez, J. M., Li, Z., Mallya, A., Hoiem, D., Jha, N. K., and Kautz, J. Dreaming to distill: Data-free knowledge transfer via deepinversion. In *Proceedings of the IEEE/CVF Conference on Computer Vision and Pattern Recognition*, pp. 8715–8724, 2020.

Zagoruyko, S. and Komodakis, N. Wide residual networks. *arXiv preprint arXiv:1605.07146*, 2016.

Zeiler, M. D. and Fergus, R. Visualizing and understanding convolutional networks. In *European conference on computer vision*, pp. 818–833. Springer, 2014.

A. Additional Results

A.1. Hyper-Parameter Tuning

Throughout the entire paper, we qualitatively selected the hyper-parameters that we choose. We randomly selected five classes of ImageNet, and performed grid searches based on visual inspection of the generated images. The following sub-section includes the set of parameters and resulting images that we used for our hyper-parameter tuning.

To tune the hyper-parameter of DeepInversion (and DeepDream) for both qualitative and quantitative examples, we used a similar grid search on all hyper-parameters. We used hyper-parameters 10x smaller, exact to, and 10x more significant than the original papers' hyperparameters. We performed visual inspections and found that these sets of hyper-parameters worked similarly well, so we used the hyper-parameters from the original papers.

A.2. Ablation Study for α and β

Figure 12 shows the results of *PII* when varying the values of α and β, which determine the intervals from which the ColorShift constants are randomly drawn. Based on this and similar experiments, we permanently fix these parameters to $\alpha = \beta = 1.0$ for all other *PII* experiments, and find that these values indeed transfer well to other models.

A.3. Insensitivity to TV regularization

Figure 13 shows additional results on the effect of ColorShift on the sensitivity to the weight of TV regularization when inverting a robust model, complementing Figure 4. As in the earlier figure, we observe that certain values of λ_{TV} may produce noisy or blurred images when not using ColorShift, whereas the ColorShift results are quite stable.

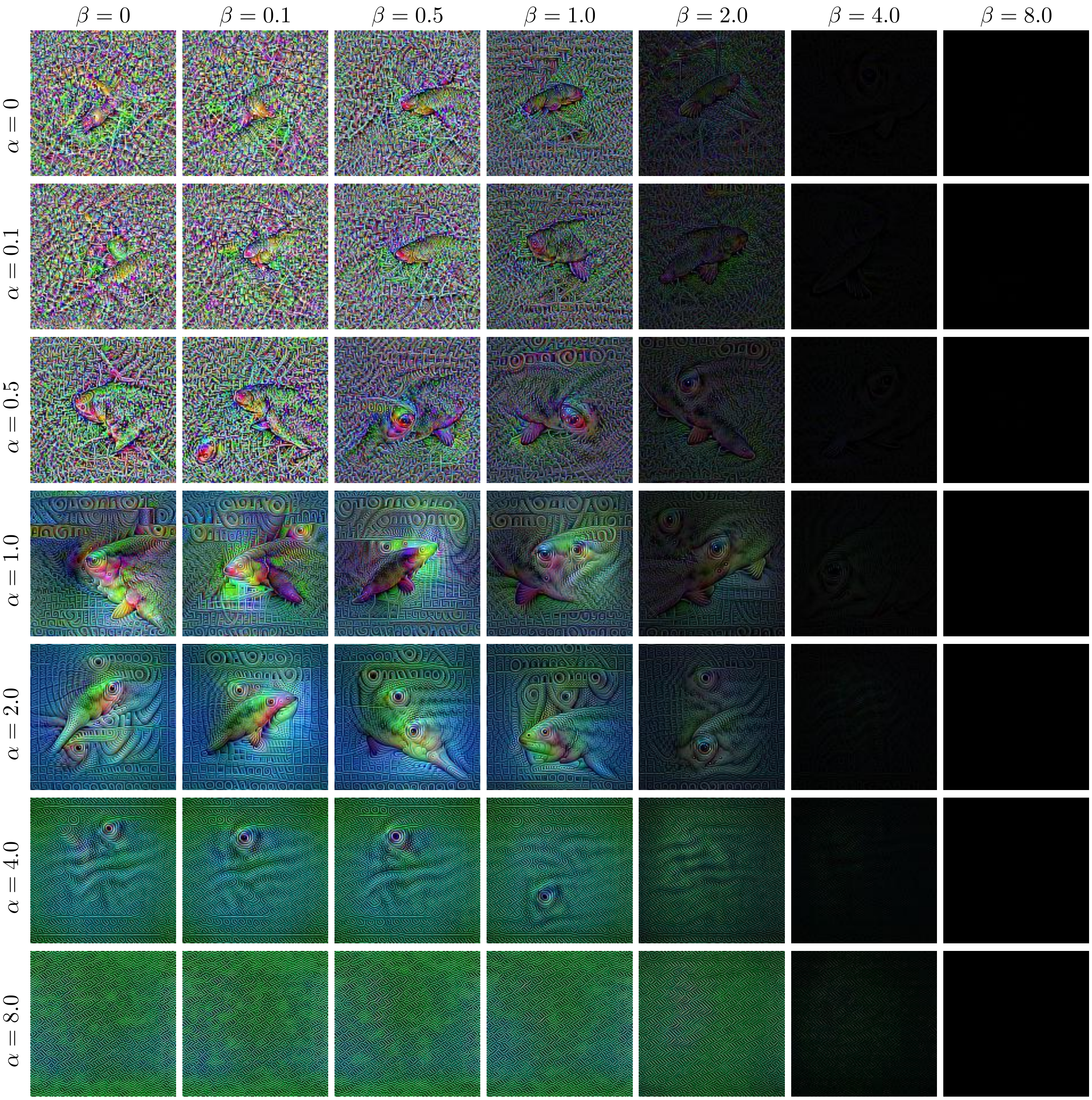

Figure 12. Effect of α and β on the quality of the images generated by *PII* from a naturally-trained ResNet-50 for the Tench class.

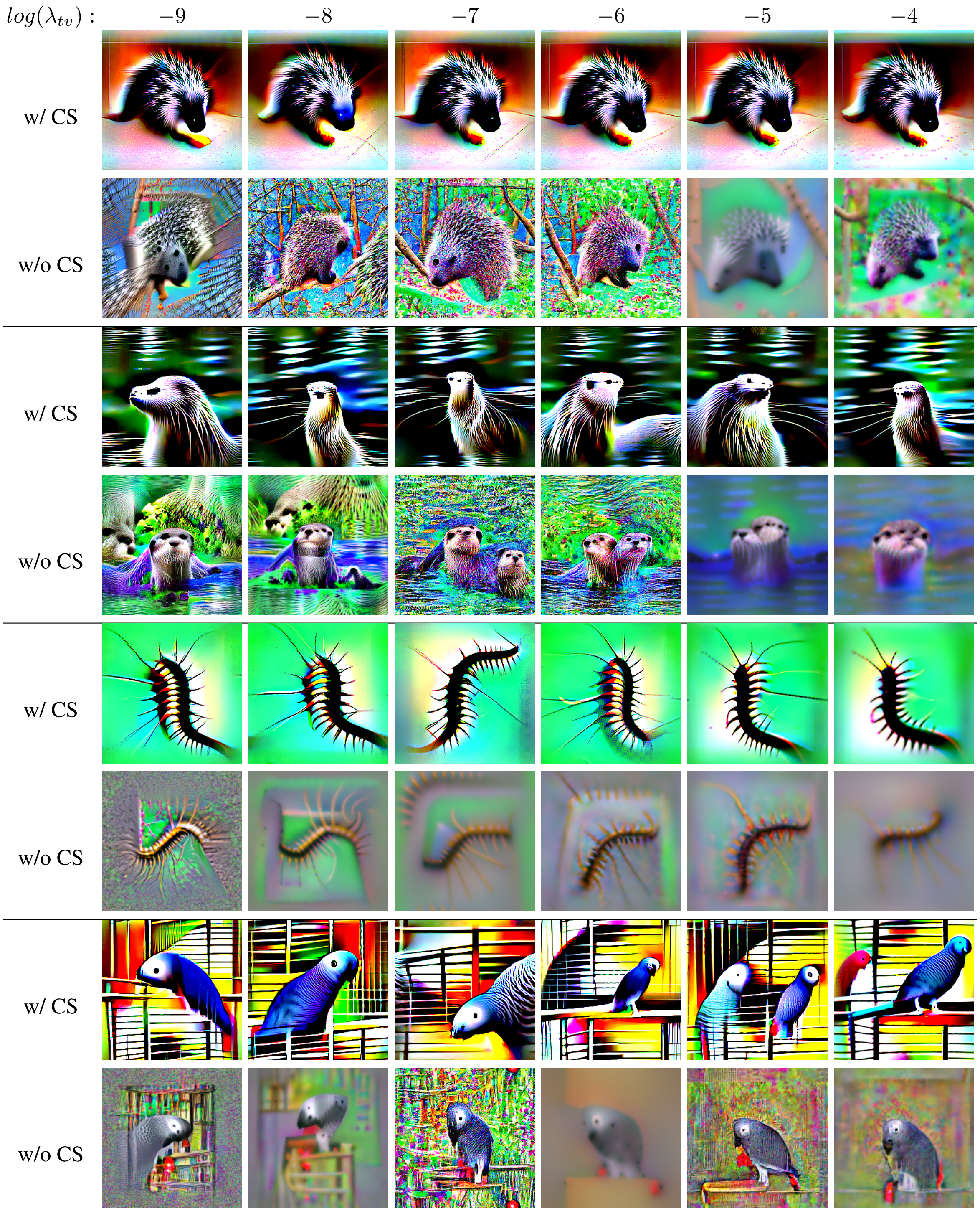

Figure 13. Effect of TV with and without ColorShift. With ColorShift it is clear that there is no need for hyper-parameter tuning for parameters such as TV. Images from the robust ResNet-50.

A.4. Effect of Centering

Figures 14 and 15 show the effect of *centering* on inverting a robust and natural model, respectively.

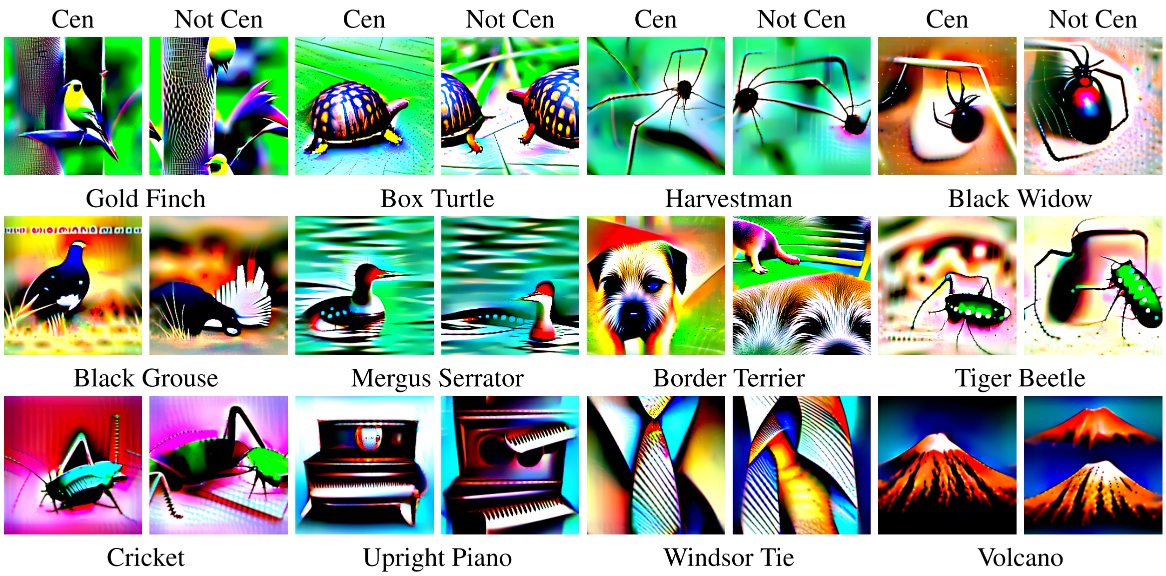

Figure 14. Effect of using centering vs not using centering for a robust ResNet-50.

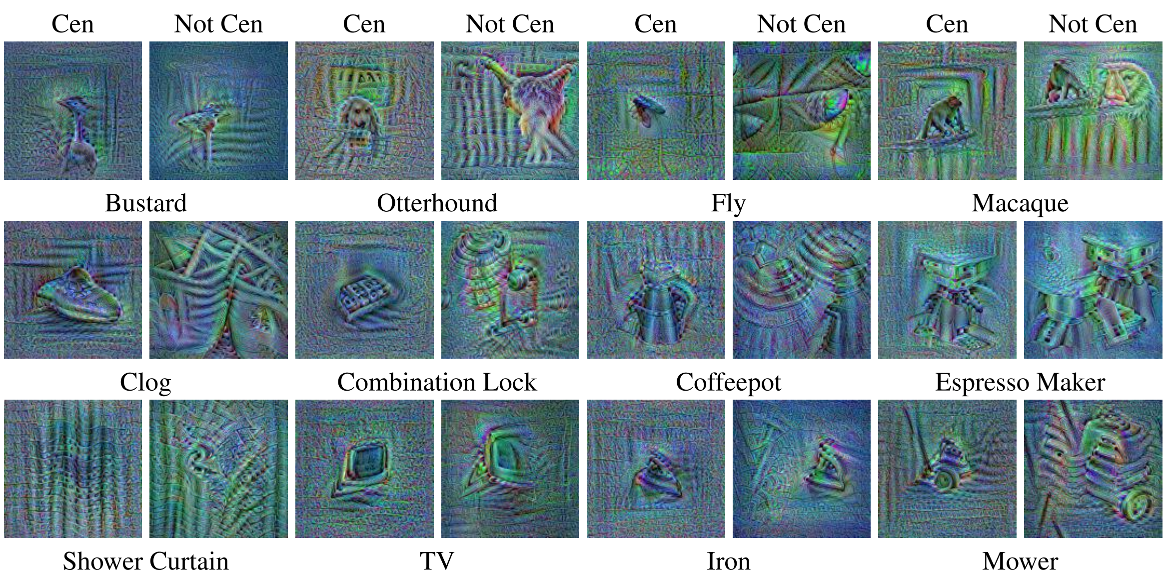

Figure 15. Effect of using centering vs not using centering for a naturally-trained ResNet-50.

A.5. Effect of Ensemble Size

Figure 16 gives additional results to those in figure 5 for the effect of ensemble size on inversion.

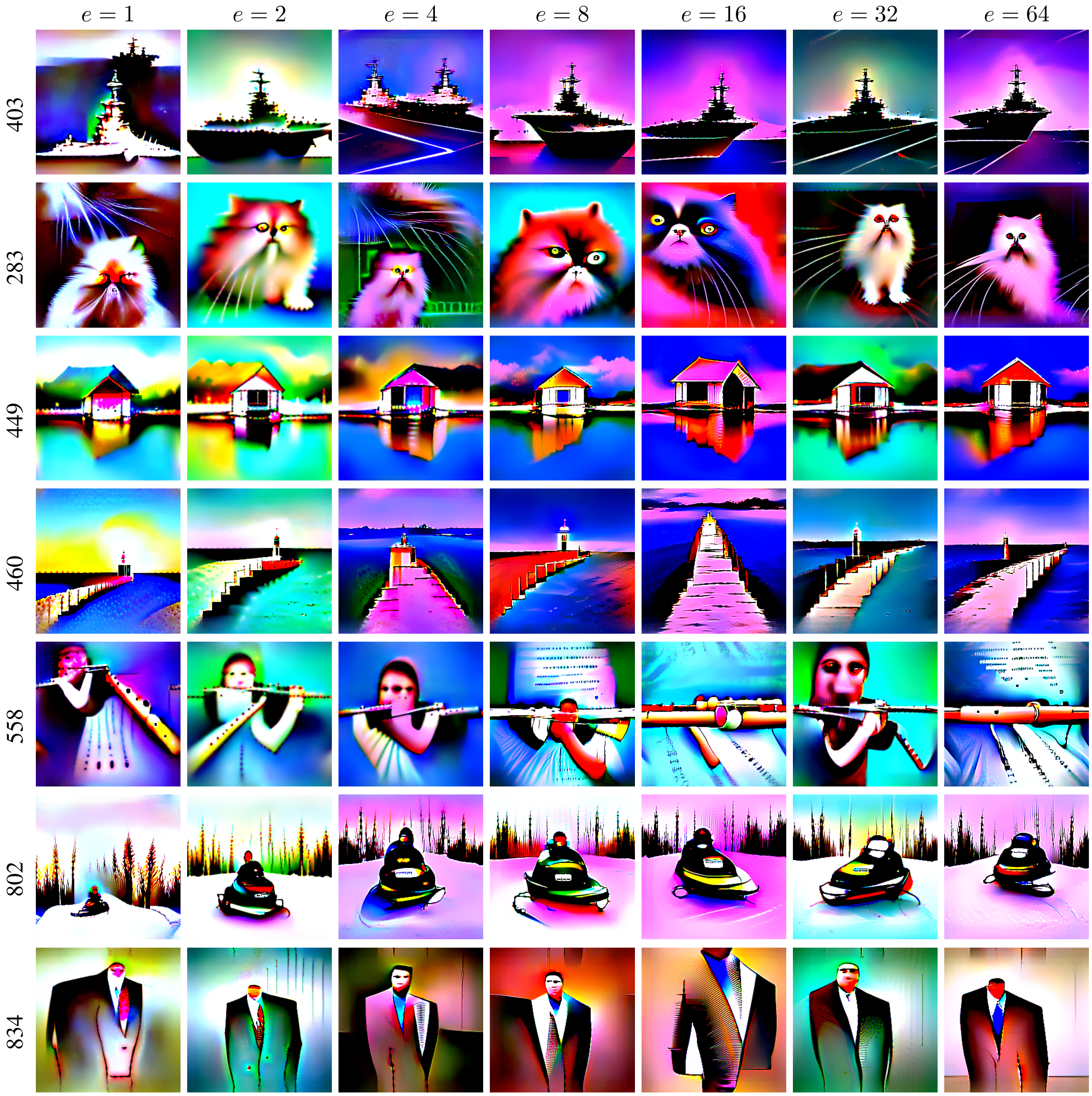

Figure 16. Effect of ensemble size when inverting a robust ResNet-50. Even small values of e give reasonably good results, but increasing e tends to give slight improvement.

A.6. Effect of using other Augmentations

We used 4 random augmentations other than ColorShift to make comparisons. We used augmentations used in (Chen et al., 2020) with modifications. We use PyTorch (Paszke et al., 2019) notation to describe this part. We used *RandomHorizontalFlip* with 0.5 probability. We used *RandomResizedCrop* with scale [0.7, 1.], and ratio [0.75, and 1.33]. With applied *ColorJitter* with 0.8 probability, and brightness, contrast, saturation, and hue of (0.4, 0.4, 0.4, 0.1), respectively. We used *RandomGrayscale* with 0.2 probability. For this experiment, we do apply data normalization before feeding the input to the network. This is different than the regular experiment setting that we use for the robust model (see appendix C). The reason is that not having data normalization is similar to using ColorShift (it changes the data distribution which the model expects as an input).

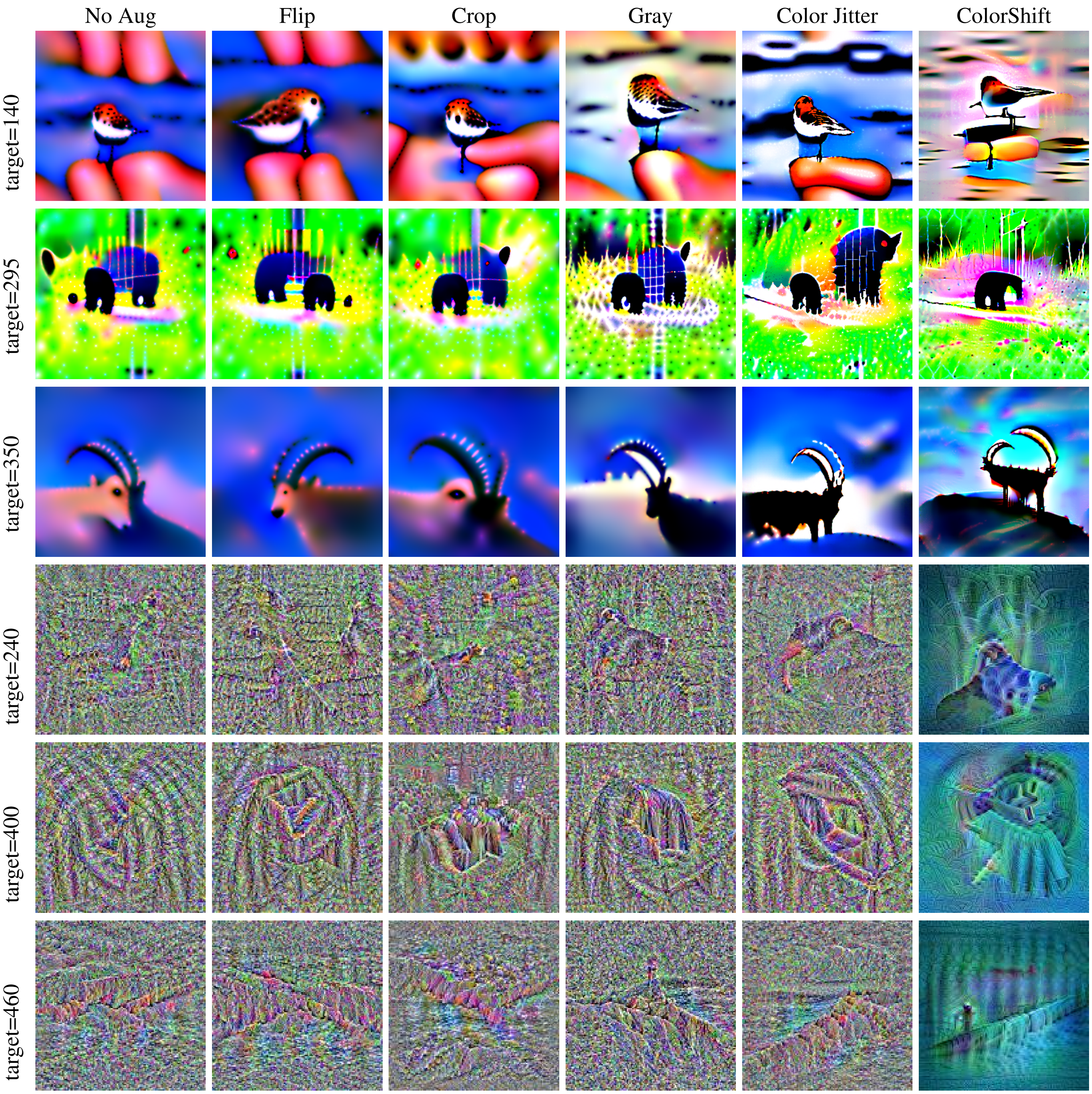

Figure 17. Effect of using different augmentations on inverting a robustly-trained ResNet-50 (top 3 rows) and a naturally-trained ResNet-50 (bottom 3 rows).

A.7. *PII* on additional networks

Figure 18 shows the results of Plug-In Inversion on various CNN, ViT, and MLP networks, adding to those shown in figure 7. See section B for model details.

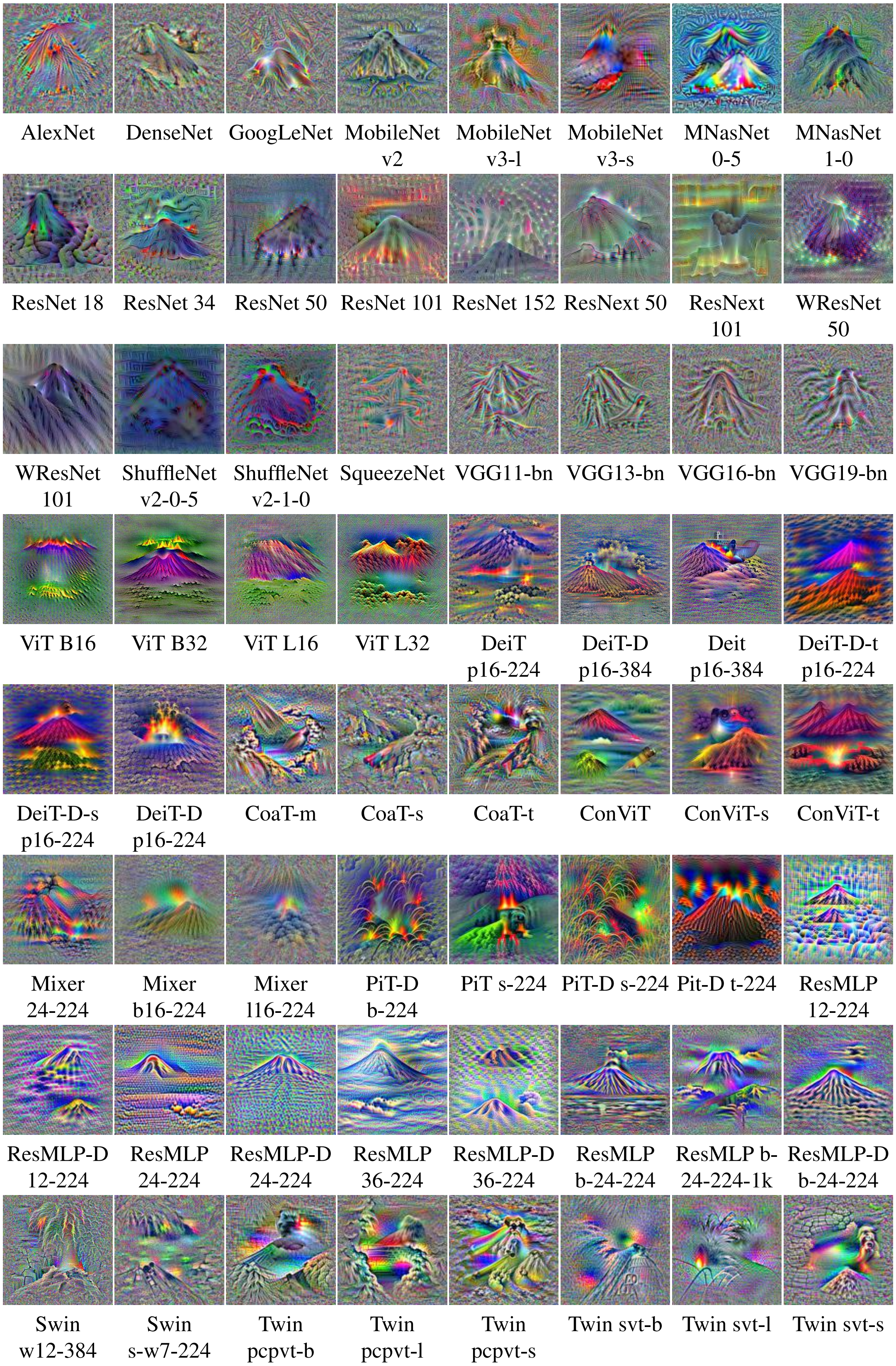

Figure 18. PII applied to various vision models for the Volcano class.

B. Models

In our experiments, we use publicly available pre-trained models from various sources. The following tables list the models used from each source, along with references to where they are introduced in the literature.

Alias	Name	Paper
ViT B16	B_16_imagenet1k	(Dosovitskiy et al., 2021)
ViT B32	B_32_imagenet1k	(Dosovitskiy et al., 2021)
ViT B-32	B_32_imagenet1k	(Dosovitskiy et al., 2021)
ViT L16	L_16_imagenet1k	(Dosovitskiy et al., 2021)
ViT L32	L_32_imagenet1k	(Dosovitskiy et al., 2021)

Figure 19. Pre-trained models used from : https://github.com/lukemelas/PyTorch-Pretrained-ViT.

Alias	Name	Paper
DeiT p16-224	deit_base_patch16_224	(Touvron et al., 2021c)
DeiT P16 224	deit_base_patch16_224	(Touvron et al., 2021c)
Deit-D p16-384	deit_base_distilled_patch16_384	(Touvron et al., 2021c)
Deit Dist P16 384	deit_base_distilled_patch16_384	(Touvron et al., 2021c)
deit p16-384	deit_base_patch16_384	(Touvron et al., 2021c)
Deit-D-t p16-224	deit_tiny_distilled_patch16_224	(Touvron et al., 2021c)
Deit-D-s p16-224	deit_small_distilled_patch16_224	(Touvron et al., 2021c)
Deit-D p16-224	deit_base_distilled_patch16_224	(Touvron et al., 2021c)

Figure 20. Pre-trained models from (Touvron et al., 2021b) .

Alias	Name	Paper
AlexNet	alexnet	(Krizhevsky et al., 2012)
DenseNet	densenet121	(Huang et al., 2017)
GoogLeNet	googlenet	(Szegedy et al., 2015)
MobileNet v2	mobilenet_v2	(Sandler et al., 2018)
MobileNet-v2	mobilenet_v2	(Sandler et al., 2018)
MobileNet v3-l	mobilenet_v3_large	(Howard et al., 2019)
MobileNet v3-s	mobilenet_v3_small	(Howard et al., 2019)
MNasNet 0-5	mnasnet0_5	(Tan et al., 2019)
MNasNet 1-0	mnasnet1_0	(Tan et al., 2019)
ResNet 18	resnet18	(He et al., 2016)
ResNet-18	resnet18	(He et al., 2016)
ResNet 34	resnet34	(He et al., 2016)
ResNet 50	resnet50	(He et al., 2016)
ResNet 101	resnet101	(He et al., 2016)
ResNet-101	resnet101	(He et al., 2016)
ResNet 152	resnet152	(He et al., 2016)
ResNext 50	resnext50_32x4d	(Xie et al., 2017)
ResNext 101	resnext101_32x8d	(Xie et al., 2017)
WResNet 50	wide_resnet50_2	(Zagoruyko & Komodakis, 2016)
WResNet 101	wide_resnet101_2	(Zagoruyko & Komodakis, 2016)
W-ResNet-101-2	wide_resnet101_2	(Zagoruyko & Komodakis, 2016)
ShuffleNet v2-0-5	shufflenet_v2_x0_5	(Ma et al., 2018)
ShuffleNet v2-1-0	shufflenet_v2_x1_0	(Ma et al., 2018)
ShuffleNet v2	shufflenet_v2_x1_0	(Ma et al., 2018)
SqueezeNet	squeezenet1_0	(Iandola et al., 2016)
VGG11-bn	vgg11_bn	(Simonyan & Zisserman, 2014)
VGG13-bn	vgg13_bn	(Simonyan & Zisserman, 2014)
VGG16-bn	vgg16_bn	(Simonyan & Zisserman, 2014)
VGG19-bn	vgg19_bn	(Simonyan & Zisserman, 2014)

Figure 21. Pre-trained models from TorchVision: https://github.com/pytorch/vision.

Alias	Name	Paper
CoaT-m	coat_lite_mini	(Xu et al., 2021)
CoaT-s	coat_lite_small	(Xu et al., 2021)
CoaT-t	coat_lite_tiny	(Xu et al., 2021)
ConViT	convit_base	(d'Ascoli et al., 2021)
ConViT-s	convit_small	(d'Ascoli et al., 2021)
ConViT-t	convit_tiny	(d'Ascoli et al., 2021)
ConViT tiny	convit_tiny	(d'Ascoli et al., 2021)
Mixer 24-224	mixer_24_224	(Tolstikhin et al., 2021)
Mixer b16-224	mixer_b16_224	(Tolstikhin et al., 2021)
Mixer b16 224	mixer_b16_224	(Tolstikhin et al., 2021)
Mixer b16-224-mill	mixer_b16_224_miil	(Tolstikhin et al., 2021)
Mixer l16-224	mixer_l16_224	(Tolstikhin et al., 2021)
PiT-D b-224	pit_b_distilled_224	(Heo et al., 2021)
PiT Dist 224	pit_b_distilled_224	(Heo et al., 2021)
PiT s-224	pit_s_224	(Heo et al., 2021)
PiT-D s-224	pit_s_distilled_224	(Heo et al., 2021)
PiT-D t-224	pit_ti_distilled_224	(Heo et al., 2021)
ResMLP 12-224	resmlp_12_224	(Touvron et al., 2021a)
ResMLP-D 12-224	resmlp_12_distilled_224	(Touvron et al., 2021a)
ResMLP 24-224	resmlp_24_224	(Touvron et al., 2021a)
ResMLP-D 24-224	resmlp_24_distilled_224	(Touvron et al., 2021a)
ResMLP 36-224	resmlp_36_224	(Touvron et al., 2021a)
ResMLP-D 36-224	resmlp_36_distilled_224	(Touvron et al., 2021a)
ResMLP 36 Dist	resmlp_36_distilled_224	(Touvron et al., 2021a)
ResMLP b-24-224	resmlp_big_24_224	(Touvron et al., 2021a)
ResMLP b-24-224-1k	resmlp_big_24_224_in22ft1k	(Touvron et al., 2021a)
ResMLP-D b-24-224	resmlp_big_24_distilled_224	(Touvron et al., 2021a)
Swin w7-224	swin_base_patch4_window7_224	(Liu et al., 2021b)
Swin l-w7-224	swin_large_patch4_window7_224	(Liu et al., 2021b)
Swin l-w12-384	swin_large_patch4_window12_384	(Liu et al., 2021b)
Swin w12-384	swin_base_patch4_window12_384	(Liu et al., 2021b)
Swin P4 W12	swin_base_patch4_window12_384	(Liu et al., 2021b)
Swin s-w7-224	swin_small_patch4_window7_224	(Liu et al., 2021b)
Swin t-w7-224	swin_tiny_patch4_window7_224	(Liu et al., 2021b)
Twin pcpvt-b	twins_pcpvt_base	(Chu et al., 2021)
Twin PCPVT	twins_pcpvt_base	(Chu et al., 2021)
Twins pcpvt-l	twins_pcpvt_large	(Chu et al., 2021)
Twins pcpvt-s	twins_pcpvt_small	(Chu et al., 2021)
Twins svt-b	twins_svt_base	(Chu et al., 2021)
Twins svt-l	twins_svt_large	(Chu et al., 2021)
Twins svt-s	twins_svt_small	(Chu et al., 2021)

Figure 22. Pre-trained models used from: (Wightman, 2019)

C. Additional experimental setting

C.1. Robust models

We use a robust RestNet-50 (He et al., 2016) model free-trained (Shafahi et al., 2019) on the ImageNet dataset (Deng et al., 2009). The setting we use for inverting robust models is very similar to that of *PII* explained in section 4 except for some differences. Throughout the paper, we use centering for robust models unless otherwise is mentioned (like when we are examining the effect of zoom and centering themselves). We use 0.0005 to scale total variation in the loss function. Also, we do not apply the data normalization layer before feeding the input to the network. In *PII* experiment setting, we apply a random ColorShift at each optimization step to each element in the ensemble. In the robust setting, we do not update the ColorShift variables μ, and σ for a fixed patch size, and we update these variables for the ensemble when we use a new patch size. Although using ColorShift would alleviate the need for using TV regularization as discussed in section 3.2, and illustrated in figure 4, we retain the TV penalty in our robust setting to make this setting more similar to that of previous inversion methods and to emphasize that it is a toy example for our ablation studies.

C.2. Comparison to DeepInversion

Similar to the original paper (Yin et al., 2020), for CIFAR-10 we use 2000 steps for the optimization. The coefficients for regularizers are set to 10.0 for the Batch-Normalization regularizer and 0.001 for Total Variation. We use ADAM optimizer with momentum parameters $\beta = (0.9, 0.999)$ and $\epsilon = 10^{-8}$. The learning rate is set to 0.1 for the entire inversion process. We use We equally invert 100 images per each class in mini-batches of size 1000. We use Jitter with maximum shift of 2 pixel along each axis as the augmentation similar to the original paper.

For the PII experiments, we optimize the images starting from images of size 8, and we increase the size of image after every 400 iterations by 4. Learning rate is initially set to 0.01 and decayed by Cosine Annealing learning rate schedule. We use the ADAM optimizer with hyper-parameters $\beta = (0.5, 0.99)$ and $\epsilon = 10^{-8}$. The learning rate and momentum parameters are set back to their original value every time the image size is increased. All other hyper-parameters are the same as ImageNet.

D. Every Class of ImageNet Dataset Inverted

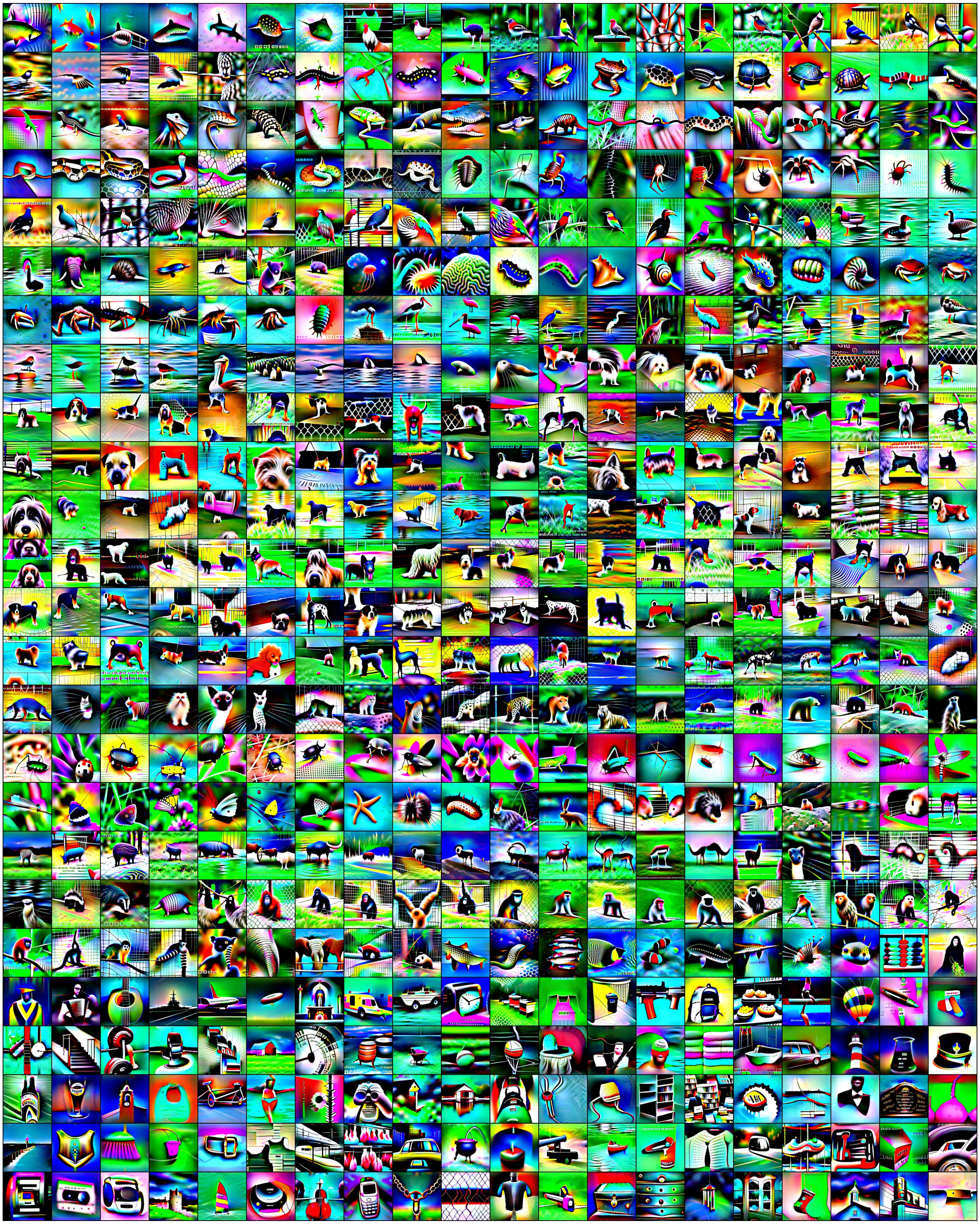

Figure 23. Inversion of first 500 classes of ImageNet for the Robust Model.

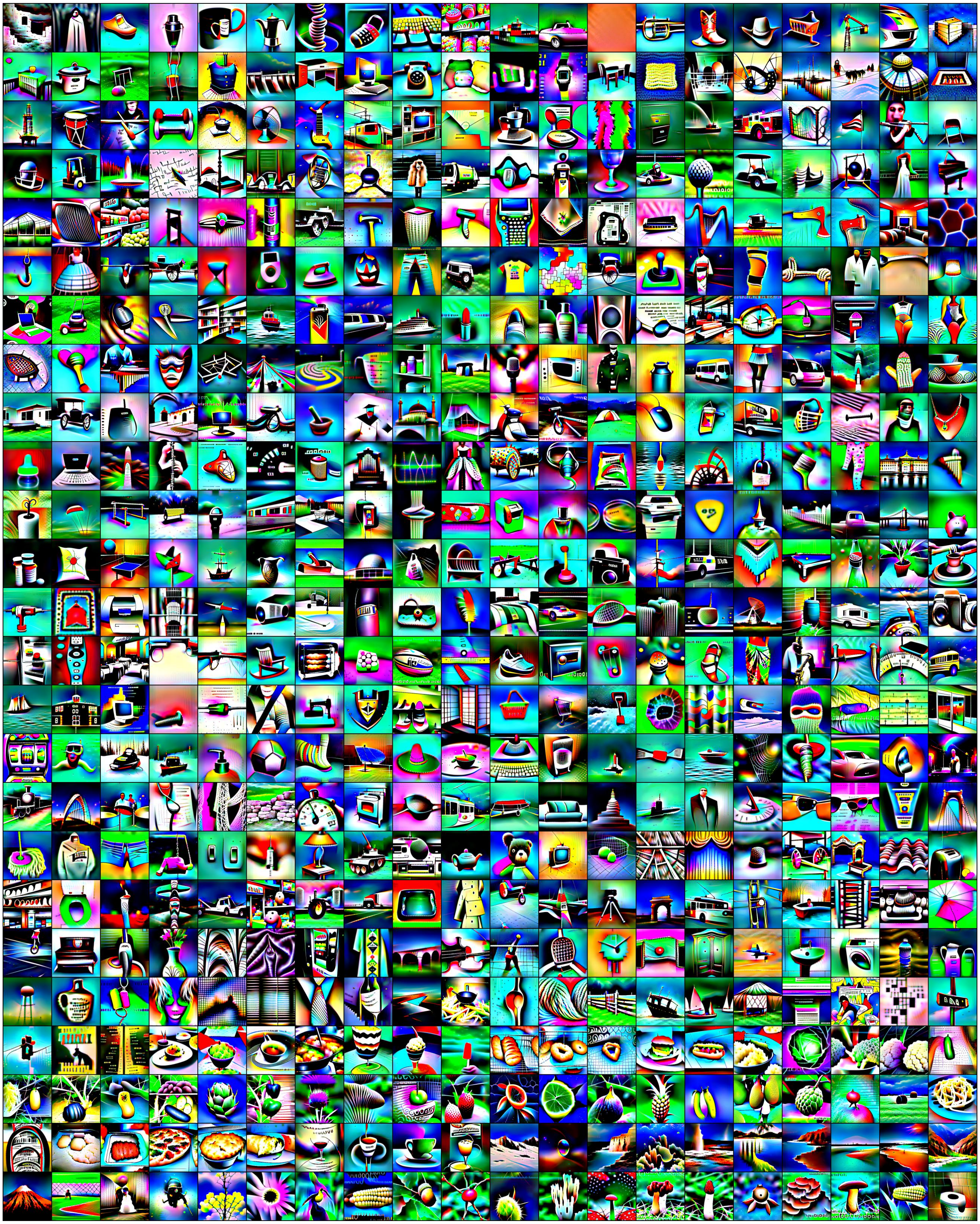

Figure 24. Inversion of second 500 classes of ImageNet for the Robust Model.

E. Optimization algorithm

Algorithm 1 Optimization procedure for Plug-In Inversion

Input: Model f, class y, final resolution R, ColorShift parameters α, β, 'ensemble' size e, randomly initialized $\mathbf{x} \in \mathcal{I}^{3 \times R/8 \times R/8}$

for $s = 1, \ldots, 7$ **do**
- Upsample $\mathbf{x}$ to resolution $\frac{(2s+1)R}{16} \times \frac{(2s+1)R}{16}$
- Pad $\mathbf{x}$ with random noise to resolution $\frac{(s+1)R}{8} \times \frac{(s+1)R}{8}$
- **for** $i = 1, \ldots, 400$ **do**
  - $\mathbf{x}' = \text{Jitter}(\mathbf{x})$
  - **for** $n = 1, \ldots, e$ **do**
    - Draw $\mu \sim U(-\alpha, \alpha)^3$, $\sigma \sim \exp(U(-\beta, \beta))^3$
    - $\mathbf{x}_n = \text{ColorShift}_{\mu,\sigma}(\mathbf{x}')$
  - $\mathcal{L} = \frac{1}{e} \sum_{n=1}^{e} NLL(f(\mathbf{x_n}), y)$
  - $\mathbf{x} \leftarrow \text{Adam}_i(\mathbf{x}, \nabla_{\mathbf{x}} \mathcal{L})$
- **return** $\mathbf{x}$

F. Additional baseline comparisons

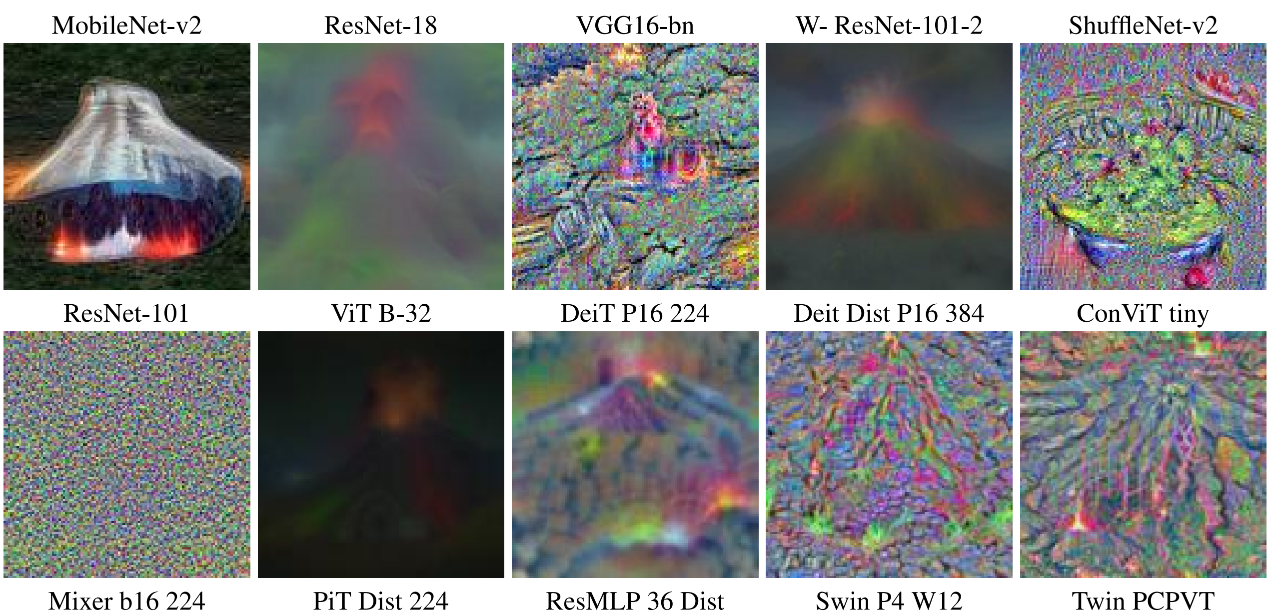

Figure 25. Images inverted from the Volcano class for various Convolutional, Transformer, and MLP-based networks using DeepInversion (CNN models) / DeepDream (non-CNN models). Cross-reference figure 7.

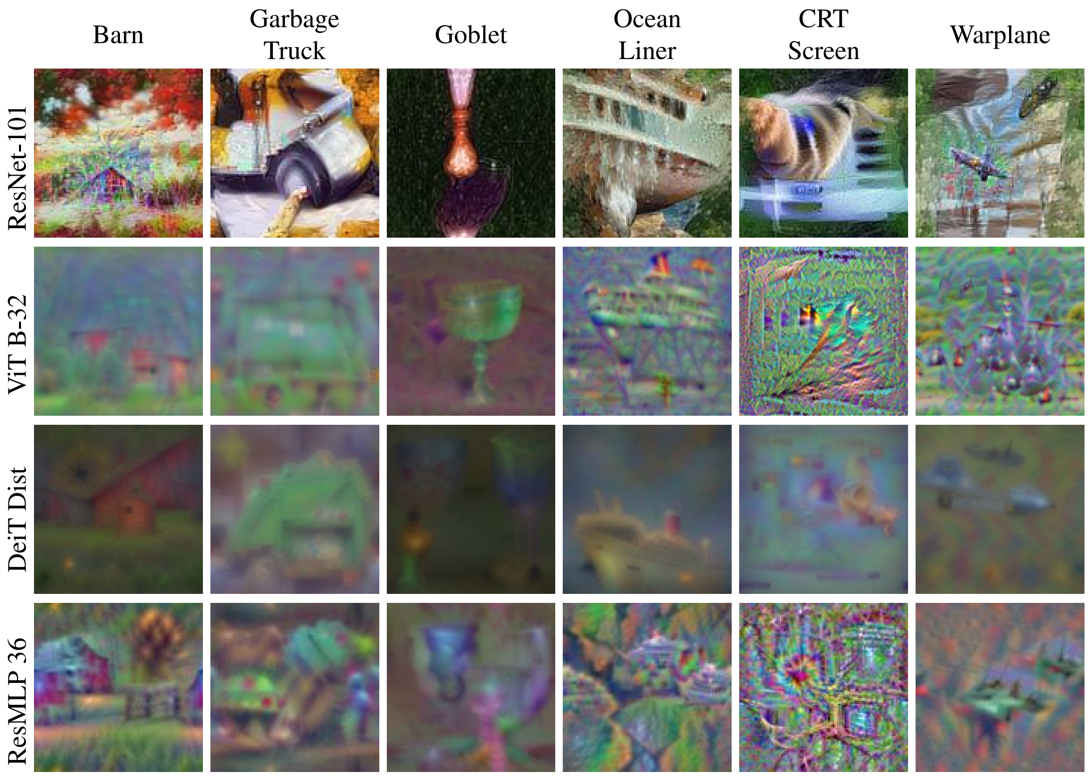

Figure 26. Inverting different model and class combinations for different classes using DeepInversion (top row) / DeepDream (other rows). Cross-reference figure 8.

G. Quantitative Results

To quantitatively evaluate our method, we invert a pre-trained ViT model to produce one image per class using *PII*, and do the same using DeepDream (i.e., DeepInversion minus feature regularization, which is not available for this model). We then use a variety of pre-trained CNN, ViT, and MLP models to classify these images. We find that every model achieves strictly higher top-1 and top-5 accuracy on the *PII*-generated image set (excepting the 'teacher' model, which perfectly classifies both). We compile these results in figure 27. Additionally, we compute the Inception score (Salimans et al., 2016) for both sets of images, which also favors *PII* over DeepDream, with scores of 28.17 ± 7.21 and 2.72 ± 0.23, respectively.

We also perform the same evaluation for images generated from a pre-trained ResMLP model. These results are more mixed; DeepDream images are classified much better by a small number of models, but the majority of models classify *PII* images better, and the average accuracy across models is approximately equal for both methods. Inception score, however, once again clearly favors *PII* over DeepDream, with scores of 6.79 ± 2.18 and 3.27 ± 0.47, respectively.

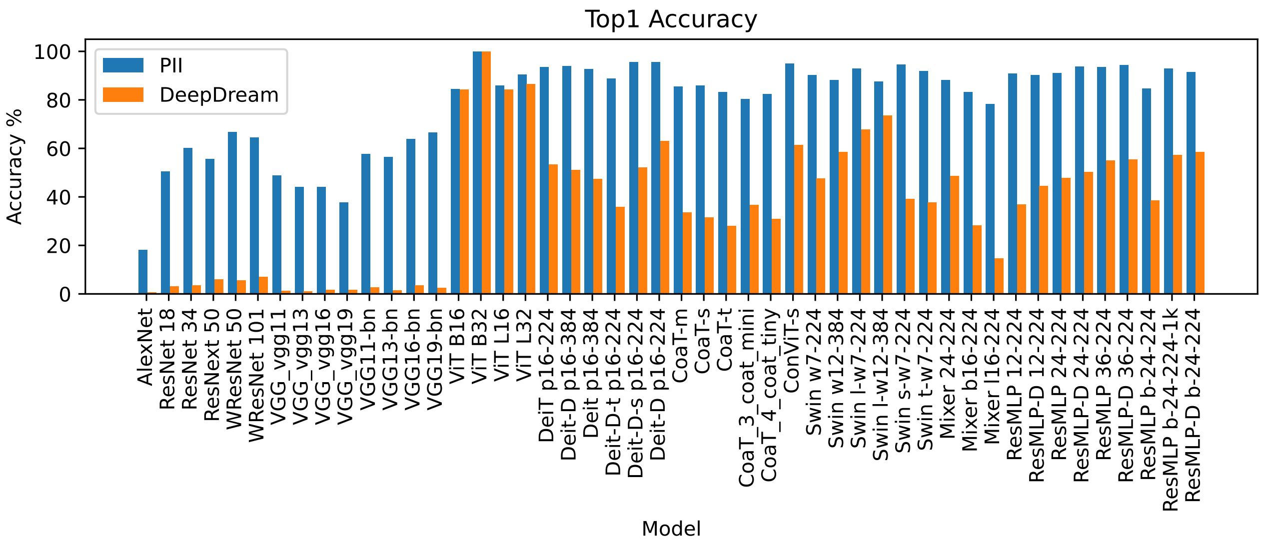

(a)

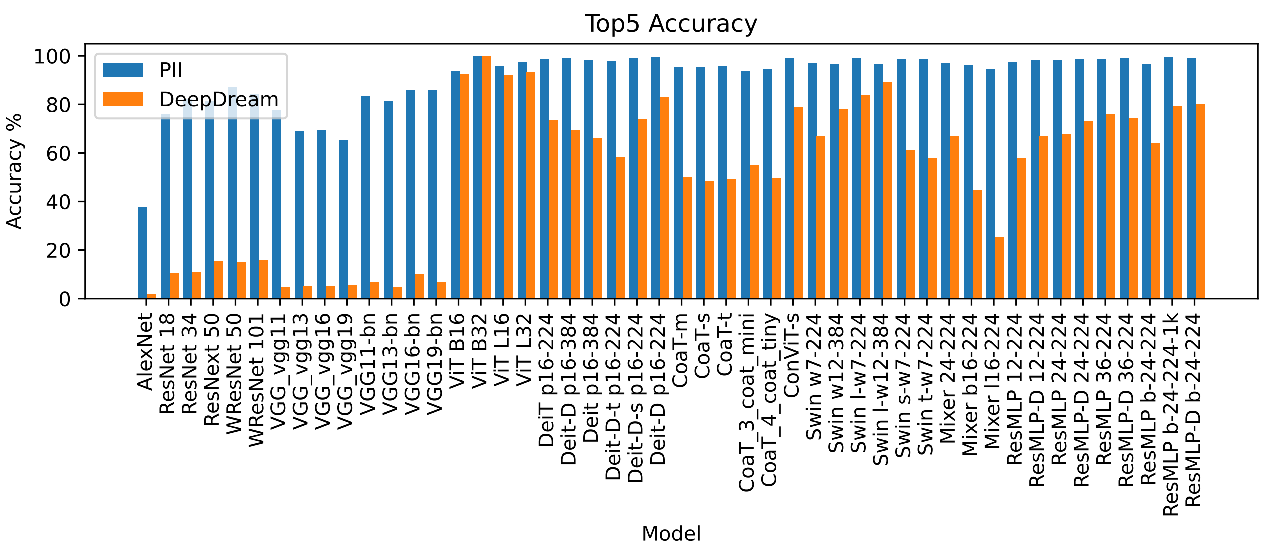

(b)

Figure 27. Top-1 (a) and top-5 (b) classification accuracy of various CNN, ViT, and MLP models evaluated on images generated from ViT B-32 using PII and DeepDream.

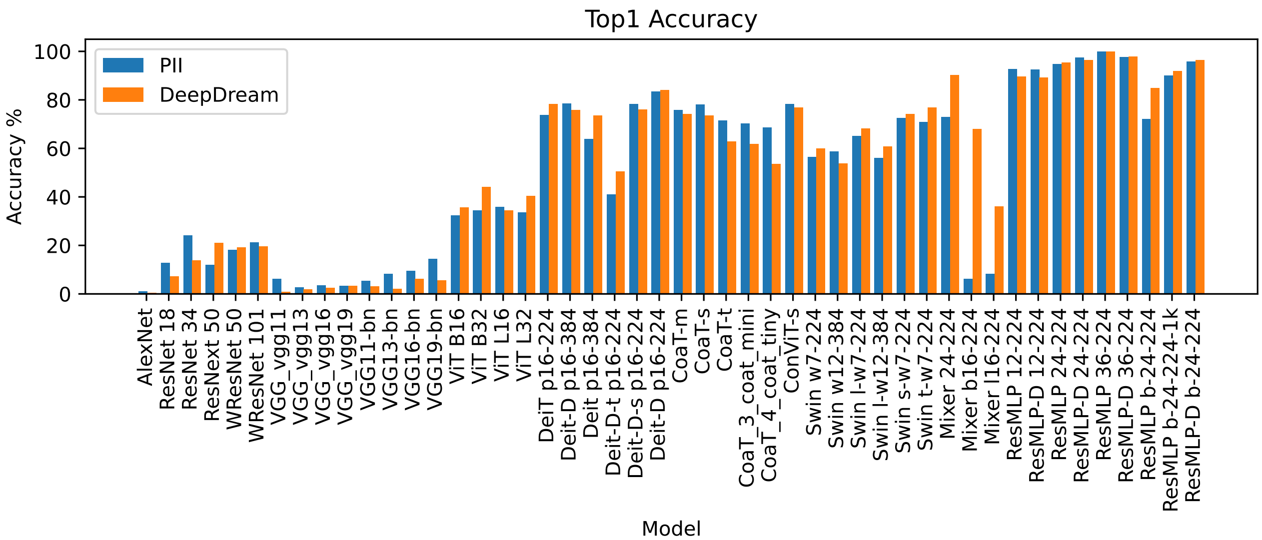

(a)

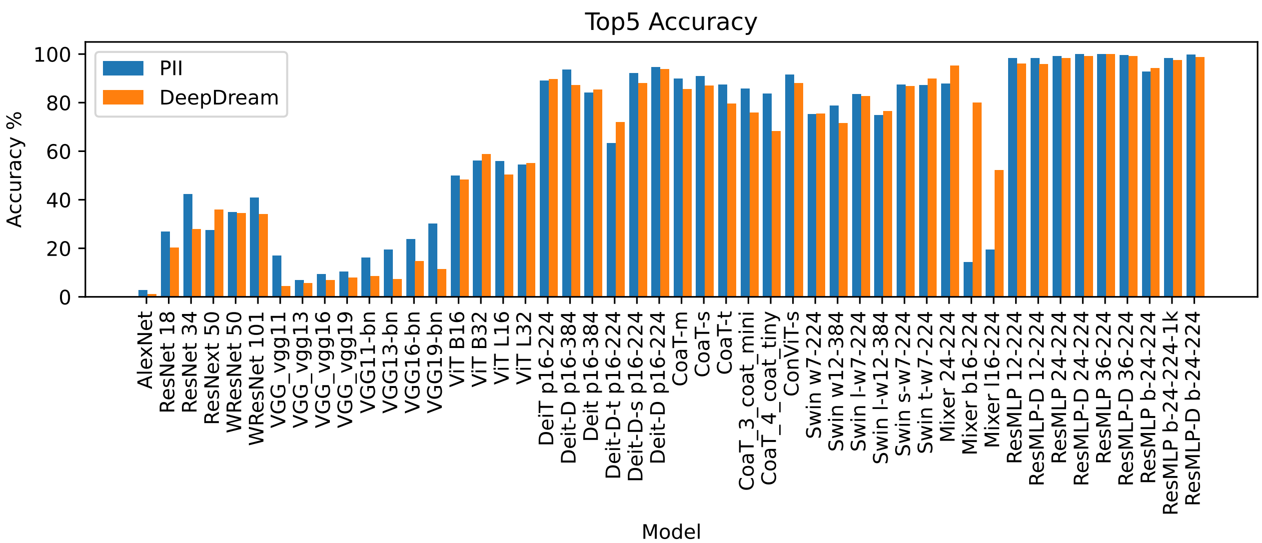

(b)

Figure 28. Top-1 (a) and top-5 (b) classification accuracy of various CNN, ViT, and MLP models evaluated on images generated from ResMLP 36-224 using PII and DeepDream.